Shear wave velocity structure beneath North-Western Himalaya and adjoining areas

Ramees R. Mir[1, *], Imtiyaz A. Parvez[1], Vinod K. Gaur[1]

[1]*CSIR – Fourth Paradigm Institute, Wind Tunnel Road, Bangalore-37, India*

[*]*Corresponding author:*
Email address: ramizmir752@gmail.com
Phone: +91 80 25051345

Note: This is a non-peer reviewed preprint submitted to *EarthArXiv*. This work was initially submitted to a scientific journal in April 2019 and was rejected after peer review. Modified afterwards, it is shared here particularly for discussion on the observation of the shallower Moho beneath the Kashmir Himalaya. Please feel free to contact the corresponding author for criticism, comments or questions.

Abstract

Shear wave velocity structure, together with Moho depths have been estimated in northwestern Himalaya, Hindu Kush and the Pamirs at a potential resolution of 0.5°×0.5° and at 1°×1° in the surrounding area, by inverting fundamental mode Rayleigh wave group velocities calculated from regional earthquake ($\Delta \leq 2500$ km) data, and also from their joint inversions with teleseismic receiver functions at 38 of the 59 broadband stations in the region that provided the data. The results yield shear-wave velocity structure of northwestern Himalaya extending from Hindu Kush through Kohistan-Nanga Parbat to Kashmir Himalaya, as well as the Pamirs in the north and Lesser Himalaya along with the foreland basin including the Hazara syntaxis in the south. In particular, shear-wave velocity profiles illuminate a) the deeper root zone structures of the main geomorphic features, b) a pervasive low velocity layer (Vs ~3.1 km/s) at ~30 km depth beneath the NW Himalaya. Another notable result is the distinctly shallower Moho beneath the Kashmir Himalaya apparently segmented by arc-normal shear zones that cross the rupture zones of the 1905 Kangra and the 2005 Kashmir earthquakes, in turn, marked by the current epoch seismicity. The obtained shear-wave velocity model of the region will be used for precise location of microseismicity, modelling strong ground motion, and as an apriori for future high resolution studies.

Keywords: North-Western Himalaya; Rayleigh-wave group velocity; shear-wave velocity structure; Moho depths.

1. Introduction

Elastic moduli and densities of materials at various depths in the earth are the most evocative descriptors of earth structure which, in turn, forms the basic perspective for formulating plausible hypotheses to model earth evolution in terms of past and ongoing tectonic processes as well as to quantify hazard. These quantities being the determinants of wave speeds, are indirectly estimated from the latter. The velocity of shear waves, in particular, proves to be a good discriminant both in relation to rigidity of the material as well as deformation induced anisotropy of rock materials at depth as proxies of past patterns of deformation. Determination of the shear-wave velocity structure of the earth at various scales and at increasing resolution in regions of complex tectonic activity such as Himalaya-Tibet, has, therefore, been the focus of seismological research since the mid twentieth century. The advent and growing expansion of broadband seismic stations around the globe, significantly advanced this trend and fueled developments of incisive analytical frameworks, notably tomographic imaging of the earth in three dimensions, which have been used in this work.

Convergence vectors in northwestern Himalaya have been found to be different from those in Central and Nepal Himalaya (Schiffman et al. 2013; Jade et al. 2020), as might be expected because of its location at the extremity of the arc, close to the Chaman-Herat transform boundary along which India slides northeastward, adding along-arc stresses to those arising from the arc-normal convergence. Schiffman et al. (2013) and Jade et al. 2020 also determined that the interseismic locked zone in northwestern Himalaya is ~145-150 km wide unlike its ~100 km width in central and Nepal Himalaya. The work presented here was motivated by the need to obtain high resolution shear velocity structure of the region spanning the northwestern extremity of the Himalaya to serve as a base-map for investigating its finer structure, carved by more complex convergence processes, notably the Moho and intra-crustal features, as well as quantification of the resulting hazard. Accordingly, we analyzed data, recorded at 59 broadband stations in and around the region (Figure 1) including 9 new ones in Kashmir Himalaya. The resulting three-dimensional shear wave velocity structure obtained by inverting fundamental mode Rayleigh wave group velocities calculated from data along 2628 criss-crossing source-receiver paths, as well as Moho depths, constitute the new results presented here.

The first such attempt for the Himalayan region as a part of the Indian subcontinent, was made by Mitra et al. (2006) who produced fundamental mode Rayleigh wave dispersion data of the region at a resolution of 7.5°. This was followed by Acton et al. (2010) who, using a larger data set which had become available by then, improved the resolution to 3°, and also obtained shear wave velocity model of India and Tibet by inverting Rayleigh wave group velocities. This work was further extended by Gilligan and Priestley (2018) who using an even larger data set, extended their coverage to include most of Asia up to 50° latitude. Their checkerboard results for the 10 sec period were able to resolve most of Himalaya and Tibet at a resolution of 2°, except the northwestern Himalaya. Recently, Li et al. (2018) made a higher resolution (0.8° × 0.8°) shear wave velocity map of the Pamir and the Hindu Kush but stopped short of the northwestern Himalaya north of the syntaxial bend. Maurya et al. (2016) also produced a 1° × 1° shear wave velocity structure of the Indian lithosphere including the Himalaya, but claimed a resolution of 200 km only. Results of this study fill the gap left by earlier ones, and shed new light on the structure of this complex region.

The 9 broadband stations installed in Kashmir Himalaya for this study, provided data for over half of the 2628 source-receiver paths, yielding fundamental mode Rayleigh wave group velocities from 8 to 60 seconds that allowed determinations of shear wave velocities over northwestern Himalaya, the Hindu Kush, the Pamir, and in the surrounding region covering the western Tarim basin, the west-central Himalaya, southern Tien Shan and western Pakistan. Shear wave velocity structure beneath 38 stations for which data were available, were also determined independently from joint inversion of teleseismic receiver functions with Rayleigh wave group velocities. These spot values compare well with those inverted from Rayleigh wave group velocities alone, showing an average correlation coefficient of 0.7 – 0.9 for upper and middle crust. Elsewhere also, in the region common with that investigated by Li et al. (2018), the correlation coefficient is ~0.7, even though the nonlinear Bayesian inverse used by us in estimating shear-wave velocities was different from that employed by Li et al. (2018). Our preference for using the Bayesian inverse was dictated by its superior performance demonstrated by comparison of inversion results (see section 2) of a data set common with that used by Maurya et al. (2016) using both the Bayesian inverse as well as the linearized least-square inversion code of Herrmann and Ammon (2004). Since, seismic network is rather sparse in the region because of challenging terranes, availability of this basic knowledge product is expected to prove helpful in designing experiments to address the many puzzles and problems of the region.

2. Data and Methodology

The data used in this study come from regional earthquakes ($\Delta \leq$ 2500 km) recorded at 59 broadband seismic stations (Figure 1). Of the 9 Kashmir Himalaya stations equipped with Nanometrics Trillium 120P broadband seismometers, all installed at hard rock sites, 3 were located on the southwestern flank of the Kashmir basin along the foothills of the Pir Panjal range, 5 around the central and northeastern Kashmir basin, and one near Drass in the Zanskar, northeast of the valley. All data were recorded at 100 samples per second and time stamped with continuous Global Positioning System with an error of the order of 10^{-3}s. Data from the international agencies of Incorporated Research Institutions for Seismology (IRIS), French Seismologic and Geodetic Network (RESIF) and German Seismic Network (GEOFON) were downloaded and preprocessed using Obspy (Beyreuther et al. 2010). The IRIS sites included, 13 broadband stations of the XG95 network (1995-1996) around Nanga Parbat, equipped with Guralp CMG-3 broadband seismometers with velocity sensitivity of 1500 Vs/m and a flat response range of 40 s -16 Hz, and one each in Kabul (KBL) and Nilore(NIL) equipped with Nanometrics Trillium 240s and STS-2 respectively. The 19 station YT network operated by RESIF from January to December 2001 were equipped with Guralp CMG-3 and STS-2 instruments, whilst the two GEOFON sites at Kabul and Aksay in Kyrgyzstan were equipped with STS-2 seismometers. Additionally, we used data from the Indian stations at Leh and Hanle installed by the Indian Institute of Astrophysics with Guralp CMG-3 instruments, and 12 broadband stations of the National Centre for Seismology (NCS). Records of the revised regional earthquakes ($\Delta \leq$ 2500 km) from the USGS (United States Geological Survey) earthquake catalog showing ≤20 km position errors were extracted as 30 minute time series. All vertical-component seismograms duly corrected for their respective instrument responses, were bandpass filtered between 0.008-0.2 Hz, and converted into the SAC (Seismic Analysis Code, Goldstein and Snoke, 2005) format.

Fundamental mode Rayleigh waveforms $S(\omega_k)$ centered at closely spaced frequencies ω_k in the band, were extracted for each source-receiver path, by filtering the corresponding Fourier domain vertical seismograms through narrow Gaussian filters $e^{[-\alpha(\omega-\omega_k)^2]/\omega_k^2}$ using the multiple filter method (Dziewonski et al.1969; Herrmann1973), where the values of α which determines the balance between the source-receiver distance and resolution, were taken from Herrmann's manual (Hermann and Ammon, 2004). The various frequency domain $S(\omega_k)$ waveforms were then transformed into their time domain $s_k(t)$ counterparts to determine their average group travel times $T_g(\omega_k)$ along a given source-receiver path, taking as reference, the maximum amplitude $a_k\left(\frac{da_k}{dt}=0\right)$ of the corresponding time domain waveform $s_k(t)$. The set of travel times $T_g(\omega_k)$ dividing the corresponding source-receiver distance, yield the Rayleigh wave fundamental mode dispersion data $V_{Rg}(\omega)$ along each of the criss-crossing vertical planes joining the various sources and receivers. These were then inverted to produce a 2 dimensional Rayleigh wave dispersion map of the region (Figures 2-3) for periods between 08 to 60 seconds, using the two step, Fast Marching Surface-wave Tomography code (FMST) of Rawlinson and Sambridge, (2005). Damping and smoothing parameters used in these inversions were chosen to be 0.5 and 1.0 respectively, after extensive tests covering a wide range (0-500) of these values. Manual picking of the fundamental mode dispersion at source-receiver distances of $\leq$ 2500 km along with the use of the FMST which computes wavefronts using a finite-difference scheme, makes the estimations more robust even in a highly heterogeneous medium, compared with the traditional ray-tracing method (Rawlinson and Sambridge, 2004), and mitigates the blurring effects of refraction and multi-pathing that begin to assume significance at source-receiver distances >5000 km (Ritzwoller et al. 2002).

In order to check the potential resolution of tomographic solutions, we performed synthetic checkerboard tests using 0.5° × 0.5° and 1.0° × 1.0° square grid anomalies with two contrasting velocities equal to $V_{Rg}(\omega)\pm 0.66$ km/s assigned to alternate grids, where $V_{Rg}(\omega)$ denotes the average of all group velocities in the region at the frequency ω. We then calculated synthetic travel times for this prescribed velocity model produced by the same source-receiver sets for which we had observed data, and inverted these, via subspace method equipped in FMST package, after contaminating each of the paths with random Gaussian noise having maximum standard deviation of 0.54s. Whilst the fidelity with which the inverted solution correlates with the originally prescribed model, in turn, determined by the azimuthal spread and density of source-receiver paths through a particular grid, is generally regarded as proof of the claimed resolution, the approach suffers from the fundamental ambiguity of inverse solutions. We further tried to minimize the uncertainties by visually demarcating the region for which the 0.5° × 0.5° anomaly recovering could be justifiably relied on, both by looking at the quality of reproduction in the inverted checkerboard solutions for various periods as well as the azimuth spread - path density data at the corresponding periods through each grid. Both these indicators for the 20 seconds period are shown in Figure 4.

We used the Neighborhood Algorithm (NA) (Sambridge1999a,b) as implemented by Yao et al. (2008) to invert the Rayleigh wave dispersion data to obtain both the shear wave velocity with respect to depth as well as Moho depths in the region. The NA performs the inversion by calculating an ensemble of a-posteriori models from a given number of a-priori models generated from a chosen one through a guided process of refinement. First, a number n_s of random versions of the a-priori model vector are generated by perturbing it by 10 - 15%, and misfits with respect to the 2-D dispersion data calculated for each of these perturbed models to produce an error (misfit) surface. The sets of least misfits in the error surface is then used to select the best fitting subset of n_r models, each demarcated by Voronoi cells (Okabe et al. 2000). Each of these n_r models is then used to generate the next suite of n_s models through (n_s /n_r) random walks in each of the n_rVoronoi cell, yielding an updated error surface. This process is iterated to home on to a set of best fitting models where-after the entire set of parent and daughter models are inverted to obtain an ensemble of a-posteriori models.

We followed Sambridge (1999a, b) by creating a first set of 300 a-priori models by perturbing the shear wave velocities of Maurya et al. (2016) beneath each grid of the region, to a maximum of ±0.8 km/s. The choice of Maurya et al's model as a basis for defining our a-priori model was dictated by the large commonality of the data sets used by us. However, since Maurya et al. (2016) had derived their shear wave velocity model from dispersion data available only above 16 sec period, we chose a higher range of perturbation (±0.8 km/s) to ensure that a larger possible model space could be sampled. A-priori values of Moho depths beneath each grid were also abstracted from Maurya et al's model by selecting the surface where the shear wave velocity crossed the 4.2 ± 0.2 km/s value (e.g., Rai et al. 2006; Hazarika et al.2017; Mir et al.2017). From this first suite of perturbed models we selected 50 best fitting ones, each demarcated in the model space by Voronoi cells and defined by its misfit value. Next, we generated 2 new models in each Voronoi cell through random walk, and isolated from amongst these, the next set of 50 best fitting models. These new points in the model space together with their parent models define a new configuration of Voronoi cells and a corresponding misfit surface, thus obtaining a total of 32,200 a-priori models after 319 iterations (Figure 5). From these we obtained an ensemble of a-posteriori models using the Bayesian Inverse. The one amongst these with the least covariance is then adopted as the final model.

Shear wave velocity structure of the region thus calculated is shown in Figure 6, whilst the Moho depths are shown in Figure 7. In order to check the reliability of this determination, we also calculated the shear wave velocity structure beneath 38 sites for which data were available, by joint inversion of teleseismic receiver functions with a weakly weighted (10%) surface wave dispersion data. These are compared for 8 stations in Figure 8. To add further constraints on shallow structures beneath the Kashmir basin, we calculated fundamental mode Rayleigh wave group velocities for 3-8 sec period by cross-correlating ambient noise on vertical components of seismograms recorded at 7 Kashmir basin stations. These data along with dispersion data from earthquakes as described above were jointly inverted with calculated RFs at the respective sites. Further, in order to appraise the relative quality of the above inversions, we also inverted the surface wave dispersion data using the linearized least-square inversion code of Hermann and Ammon, (2004) with two initial models: a modified AK135 model with a constant velocity of 4.48 km/s from the surface down to 100 km, and the shear velocity model of Maurya et al.(2016). Compared with the result of the Bayesian inverse, both the other solutions were found to produce a smoother structure blurring even the prominent geomorphic features.

Moho being a prominent discontinuity in the earth, its depth determines the Rayleigh wave dispersion, in addition to the average crustal shear wave velocity. Accordingly, Moho depths in the region were estimated by inverting Rayleigh wave group velocities beneath each point of the grid, using the 4.4 km/s surface in Maurya et al's shear wave structure for the region, as an a-priori Moho, and allowing it to excurse within 4 km of this depth to seek the best fit. Posterior Moho depths, thus determined with maximum uncertainty of ±2.6 km, are shown in Figure 7 along with its similarly color coded spot values determined by various authors (see section 3.3) from inversion of receiver functions, some jointly with surface wave dispersion data. The divergence between the map and the spot Moho values are generally seen to lie within these uncertainties and vouch for confidence in the reliability of these estimations.

3. Results

The paper presents three sets of maps at 0.5° × 0.5° grid corners covering the northwestern Himalaya, the Hindu Kush and the Pamirs, and at 1° × 1° grid points for the surrounding areas (Figure 1). These are i) Rayleigh wave dispersion maps for 8-60 sec periods (Figures 2, 3), ii) shear wave velocity maps (Figure 6) up to a depth of 80 km, and iii) Moho depth maps beneath the entire region (Figures 7).

3.1 Dispersion maps

Grid-wise Rayleigh wave group velocity maps for the region were calculated from fundamental mode Rayleigh waves for 10 different periods between 8 and 60 s. Five of these between 10 and 50 seconds are shown in Figures 2 and 3. Apart from clear identification of the low velocity enclaves of western Tarim, Tadjik and the Himalayan foreland basins with the sediment thickness map (correlation coefficient of -0.76 to -0.98) (Figure 2b) of *Laske and Masters,* (1997), the 10 and 20 sec maps also delineate the high velocity southern margin of the Hindu Kush extending to the slightly lower velocity northwestern Himalaya from Nanga Parbat to Himachal and Pamir to Tien Shan. Equally clearly, the latter define the Kunlun – AltynTagh Fault (ATF) in the northeast and the Lesser Himalayan front in the south, across which velocities are lower. In fact, the map captures even the eastern Tarim basin, the western Tadjik basin, the northern Indus basin and the Fergana basin that lie well outside our well resolved region. The northwest-southeast trending Himalayan terrain northeast of the foreland basin is clearly marked by higher velocity at all periods whilst Tibet to its northeast, is significantly low at periods higher than 30 seconds. A notable feature brought out by the shallow (10-30 sec) dispersion maps is a high velocity (~3.1-3.2 km/s) enclave that geographically coincides with the location of the higher density gneissic complexes of the northwestern Aravalli craton in peninsular India. This anomalous region lies far to the south of our well resolved region, suggesting that it might be an artefact. To check this possibility, we carried out a spike test, centered at this anomalous area. The corresponding inverted solution is shown in Figure A2 and compared with a similar spike test centered at a point in the well resolved area. The map shows that whilst the recovery of the former is only in the form of a diffused halo as expected from its location outside the well resolved region, its unmistakable identification with the northwestern core of the Aravalli craton at least up to periods of 20 seconds, testifies to the robustness of our maps.

3.2 Shear-wave velocity structure

The second set is the shear wave velocity structure of the region between 10-80 km depth (Figure 6) derived from the aforesaid dispersion maps. These were tested at 38 points of the region against alternatively calculated shear wave velocity structure inverted by joint inversion of surface wave dispersion data and teleseismic receiver functions. Eight of these are shown in Figure 8. These figures distinguish 6 tectonic features of the region: The Hindu Kush and its high velocity suture-zone oceanic crust bordering the subducting Indian lithosphere, the Nanga Parbat and its Himalayan extension to the east, the Pamirs north of the Nanga Parbat syntaxis, Tibet, the Tarim basin, and the Himalayan foreland basin. At 10 km, high shear velocities (~3.4 km/s) mark out the Hindu Kush subduction zone, the Pamirs and the northwestern Himalaya against the ~3.1 km/sec foreland basin, albeit with a small variance, but the deeper higher velocity (~3.8 km/s) cores of these features become more sharply defined at 20 km. At 30 km the entire northwestern Himalaya and Hindu Kush is characterized by low velocities (~3.2 km/s) except for the Pamirs where the velocity reversal to a lower value occurs at ~40 km, whilst the western Tarim basin to the northeast and the Himalayan foreland basin exhibit higher (~4.0 km/s) velocities, likely representing the oppositely underthrusting Asian and Indian plates respectively. Further down beneath Pamir, shear velocities decrease whilst they continue increasing beneath Nanga Parbat up to a depth of 60 km - the limit of our resolution. Another high velocity enclave also appears at this depth around the Hazara syntaxial (HS, Figure 1) bend of the Lesser Himalaya.

The generation of 32200 models at each grid point with allowed Vs variation of ±0.8 km/s around the model parameters of Maurya et al.(2016) taken as an a-priori model, resulted in a rich suite of posterior models using NA, whose error estimates, being free from the bias introduced by regularization parameters, are expected to be more robust. Posterior error estimates for each of the maps in Figure 6, which are < 0.45 km/s up to a depth of 70 km in the well resolved region, and < 0.46 km/s up to 60 km depth in the surrounding region, are shown in Figure A3. Shallower enclaves of high velocity beneath the Hindu Kush, Pamir, NangaParbat (10-20 km) have a maximum posterior error of 0.25 km/s, as also the low velocity layers observed at 30 km beneath the Hindu Kush and NW Himalaya and at 40-50 km beneath the Pamirs. For Kashmir Himalaya, which contributes more than 50% of the data used in this study, the maximum error in Vs is < 0.4 km/s to a depth of 100 km.

3.3 Moho depth

The third set of maps shows Moho depths beneath the region (Figure 7) as well as Moho depth variations along 6 profiles of the region (Figure 9) against the background of the corresponding shear velocity structure. These are the best fitting surfaces H(x,y) that reproduce the observed dispersion $V_{Rg}(\omega)$ of fundamental mode Rayleigh waves, whilst conforming with the horizon where the shear wave velocity is 4.2 ± 0.2 km/s. Figure 9 also compares these Moho depths with those obtained in earlier studies (Figure 7; Hazarika et al. 2014,2017; Gilligan et al. 2015; Priestley et al. 2019; Rafi et al. 2019; Schneider 2014; Sharma et al. 2019), some using joint inversion of receiver functions with surface wave dispersion data. Our results, however, conform with Moho depths of the global CRUST1.0 model (Laske et al. 2013) only for NW Himalaya, Ladakh, western Tarim basin and Himalayan foreland basin (Figure A4). The most notable feature of Figure 7 is the along strike shallowing of Moho depths beneath the Kashmir Himalaya which beneath the Indus suture zone is ~10 km shallower compared with its depth beneath arc-normals both east and west of the Kashmir basin.

4. Discussion

The paper presents high resolution maps of i) fundamental mode Rayleigh wave group velocities, ii) the shear wave velocity structure and iii) Moho depths beneath the northwestern Himalaya, the Hindu Kush and the Pamir including the Himalayan foreland basin and the Hazara syntaxis (Figure 1). A larger surrounding region also shows these 3 maps at lesser resolution but degrades beyond the red boundary in Figure 1. The latter, whilst reproducing prominent features also delineated by the most recent high resolution images of a part of this region (*Li et al.* 2018), add further details, particularly to the deeper structure of southern Pamir. Notable new results indicated in the dispersion maps but better delineated in the derived shear velocity maps, highlight the higher shear wave velocity (~3.4 km/s) enclaves around a) the Hindu Kush-Kohistan, b) the Nanga Parbat extending east-southeastwards to cover northwestern Himalaya, c) the Pamirs and, d) the Ladakh batholiths, that monotonically increase right up to the Moho (4.2-4.6 km/s), except for depth limited transitional reversals to ~3.3-3.4 km/s, at 40 km beneath the Pamirs and at 30 km in the region to its south (Figure 6).

4.1 Intra-crustal low velocity layer

The pervasive shear velocity reversal at ~30 km beneath the entire northwestern Himalaya east of the Hindu Kush, albeit reported for some other regions of the Himalaya (e.g., Guo et al. 2009; Hazarika et al. 2014; Gilligan and Priestley 2018), appears counterintuitive. Its existence, if true, would be expected to play a significant unifying role in the kinematics of the Himalaya. Since we found clear signatures of this low velocity intra-crustal layer both in the surface wave dispersion derived shear velocity structure of northwestern Himalaya and also in the joint inverse solutions of receiver functions (e.g. Figure 8 B,C,E), we made intensive forward modelling tests all of which required its existence to fit the data, even as we have no means of discriminating between the various hypotheses speculated to explain its occurrence such as fluidization or occurrence of low velocity mineral phases.

4.2 High shear-wave velocity enclaves

The nearly identical shear velocity structure of the Hindu Kush, North-western Himalaya and Ladakh, delineated by the Chaman-Herat Faults (CF, HF; Figure 1) that longitudinally bisects the Hindukush, and the Main Karakoram Thrust skirting the Nanga Parbat to Ladakh, clearly outlines the northern limits of the buried Indian crust. However, the 3 high velocity enclaves of the Indian plate have differing structural settings. The westernmost Hindu Kush - Kohistan region is expected to be bordered on the northwest by the obducted Tethys ocean crust (Searle et al. 2001) that has apparently crept further southeastward giving the upper 20 km crust of the area its higher velocity character. The higher velocity signature of northwestern Himalaya, locally intensified beneath Nanga Parbat, on the other hand, reflects the existence of the wedge of Indian plate Proterozoics and crystallines detached from the underthrusting Indian plate and stacked up by the southward advance of Tibet over the Indian plate. Nanga Parbat with surface exposures of migmatites and granulite grade rocks requiring rapid exhumation and showing field evidences of along arc compression (Schneider et al. 1999), likely represent a modification of this process caused by compressional stresses imposed by the nearby Herat transform fault at the western extremity in conjunction with the likely existence of a NE-SW salient in the Indian plate thrusting underneath it. The possible role of a low viscosity region beneath Nanga Parbat in facilitating its past rapid rise has been discounted by Schneider et al. (1999) on the basis of their field mapping that showed no evidence of any significant structure that would allow the implied large scale tectonic denudation. The nature of the low velocity material at ~30 km beneath the region, its origin and role in the kinematics of the Himalaya, therefore remains obscure as that of 'the mid-crustal conductor' at ~10-25 km depth beneath Nanga Parbat mapped by Park and Mackie (1997).

The third prominent high velocity enclave represents the Ladakh batholith formed by subduction of the Neo-Tethyan oceanic crust beneath the Eurasian plate. Field observations by Kumar (2008) show that these calc-alkaline granitoids have been formed by several batches of coeval mafic and felsic magmas. The higher surface shear velocity (3.4 – 3.7 km/s) of this feature indicates a higher mafic content albeit with variations along the range to the southeast.

Figure 6 also shows that the Hazara syntaxial region and the Potwar plateau to its southwest, where shear velocities are low (2.9 – 3.1 km/sec) in the first 20 km, but, deeper down, increase (~3.8 -4.0 km/s) upto 50 km. Below this depth, the Potwar plateau immediately to its southwest, is characterized by even higher velocities (4.5-4.8 km/s) indicating the presence of a sharp rigid salient of the underthrusting Indian plate. The arc normal swath connecting Nang Parbat and the Hazara syntaxis and extending southwestward into the northern Potwar plateau, which is seismically exhibited as a shear zone (Figure 1, inset) was most likely responsible for the creation of the Hazara - Nanga Parbat syntaxes, assisted by the arc extremity compression whose field expressions are clearly manifest in the Naga Parbat (Schneider et al., 1999)

4.3 Moho depth

Along- strike Moho depths in the region beneath the Indus-suture/Main Mantle Thrust, taken as a reference, require the Moho to be shallower beneath the Kashmir Himalayan segment (Figures 7, 9).This segment, bounded by arc-normals that pass through the rupture zones of the 1905 Kangra and the 2005 Kashmir earthquakes which define the current epoch seismic gap, has not been ruptured by even a moderate earthquake since 1555. Indeed, the western boundary of this shallower Moho segment coincides with the line of earthquakes (inset in Figure 1) marking the apparently high strain Hazara-Nanga Parbat syntaxes which may be a fault or flexure. However, the eastern boundary of this shallow Moho segment, crossing the rupture zone of the 1905 earthquake, which is highlighted by a cluster of moderate and small earthquake ruptures, has no earthquake signatures further towards the Main Mantle Thrust. In any case, these bounding arc-normals, would be expected to accommodate the shallower dipping Indian plate between them through warped shear zones, which has significant pointers to model possible rupture scenarios for quantifying seismic hazard in the region. Notably, the inferred shallow dip of the Kashmir Himalaya Moho, shown by this work, clearly explains the wider interseismic locked zone observed by Schiffman et al. (2013).

5. Conclusion

In conclusion, we summarize the following salient features of the crust beneath the NW Himalaya and adjoining regions. Firstly, dispersion maps clearly mark the low velocity enclaves of western Tarim, Tadjik and the Himalayan foreland basins, showing strong correlation (-0.76 to -0.99) with the sediment thickness map of Laske and Masters (1997). Shallower dispersion maps (10-20 sec) also delineate the high velocity southeastern margin of the Hindu Kush (V_{Rg} ~3.3 km/s) extending to the slightly lower velocity northwestern Himalaya (~3.1 -3.2 km/s). On dispersion maps higher than 30 sec Tibet and northeastern regions are marked by low (~2.7-3.0 km/s) velocities, apparently representing the thicker crust underneath.

Secondly, the inverted shear wave velocity maps clearly demarcate the shallower structures which have strong geomorphic signatures. For example, at 10 km, high shear velocities (~3.4 km/s) mark out the Hindu Kush subduction zone, the Pamirs and the northwestern Himalaya, while low velocities mark the sedimentary basins of Tadjik, western Tarim, and Himalayan foreland basin (~3.1 km/s). The high velocities correspond to surface location of high grade crystallines in the Nanga Parbat, gneiss domes in the Pamirs, the obducted Tethys ocean crust in the Hind Kush, and subduction of the Neo-Tethyan oceanic crust beneath the Eurasian plate in Ladakh. At 30 km the entire northwestern Himalaya and Hindu Kush is characterized by low velocities (~3.2 km/s) except for the Pamir (~3.7 km/s); such layer(s) have also been reported for other regions of the Himalaya (e.g. Guo et al. 2009; Gilligan and Priestlely 2018). Existence tests for this pervasive layer were done by intensive forward modeling all of which required its existence to fit the data. The deeper (40-60 km) high velocity signature beneath Nanga Parbat, reflects the existence of the wedge of Indian plate Proterozoics and crystallines detached from the underthrusting Indian plate and stacked up by the southward advance of Tibet over the Indian plate.

Finally, we estimate posterior Moho depths beneath the region. The most notable feature reported here is the along strike shallowing of Moho depths beneath the Kashmir Himalaya which beneath the Indus suture zone is found to be ~10 km shallower compared with its depth beneath arc-normals both east and west of the Kashmir basin, and explains the wider interseismic locking zone reported by Schiffman et al (2013), Jade et al. (2020). Further, this segment is clearly bounded by arc-normals that pass through the rupture zones of the 1905 Kangra and the 2005 Kashmir earthquakes which define the current epoch seismic gap that has not been ruptured by even a moderate earthquake since 1555. Results of this study fill the gap left by earlier ones and shed new light on the finer structure of this complex region. Availability of the shear wave velocity database, illuminated the above discussed features, and is further expected to prove helpful in designing experiments to address the many problems of the region e.g. nature of the Moho upwarp in NW Himalaya, quantification of the hazard.

Acknowledgments

This study was supported by the project GAP-1010 of the Ministry of Earth Sciences,Government of India. We gratefully acknowledge the logistics support provided by Professor Talat Ahmed, Rakesh Chandra and Shakil Romshoo of the University of Kashmir in the installation of seismic stations at various sites in Kashmir Himalaya. We thank Satish Maurya for providing the velocity models from Maurya et al. (2016). RM would like to thank Ashish for deployment of the instruments in the field and Gokul Saha for essential inputs during initial stages of this work. Availability of the data freely shared by the various national and international agencies, the NCS, IRIS, GEOFON and the RESIF, is deeply appreciated. Figures were generated using the Generic Mapping Tools (Wessel et al., 2013) and the S-plot/NA-plot routines of Sambridge (1999a,b). Topography data were taken from Amante and Eakins, (2009) (January, 2017). Data queries shall be addressed to IAP (parvez@csir4pi.in).

Author Contributions

IAP and VKG designed the Kashmir broadband seismic experiment. RRM executed the installation and servicing of the broadband sites, with support from IAP, and performed all the data analysis. RRM produced the first draft which was developed to its present form by contributions made by all the authors.

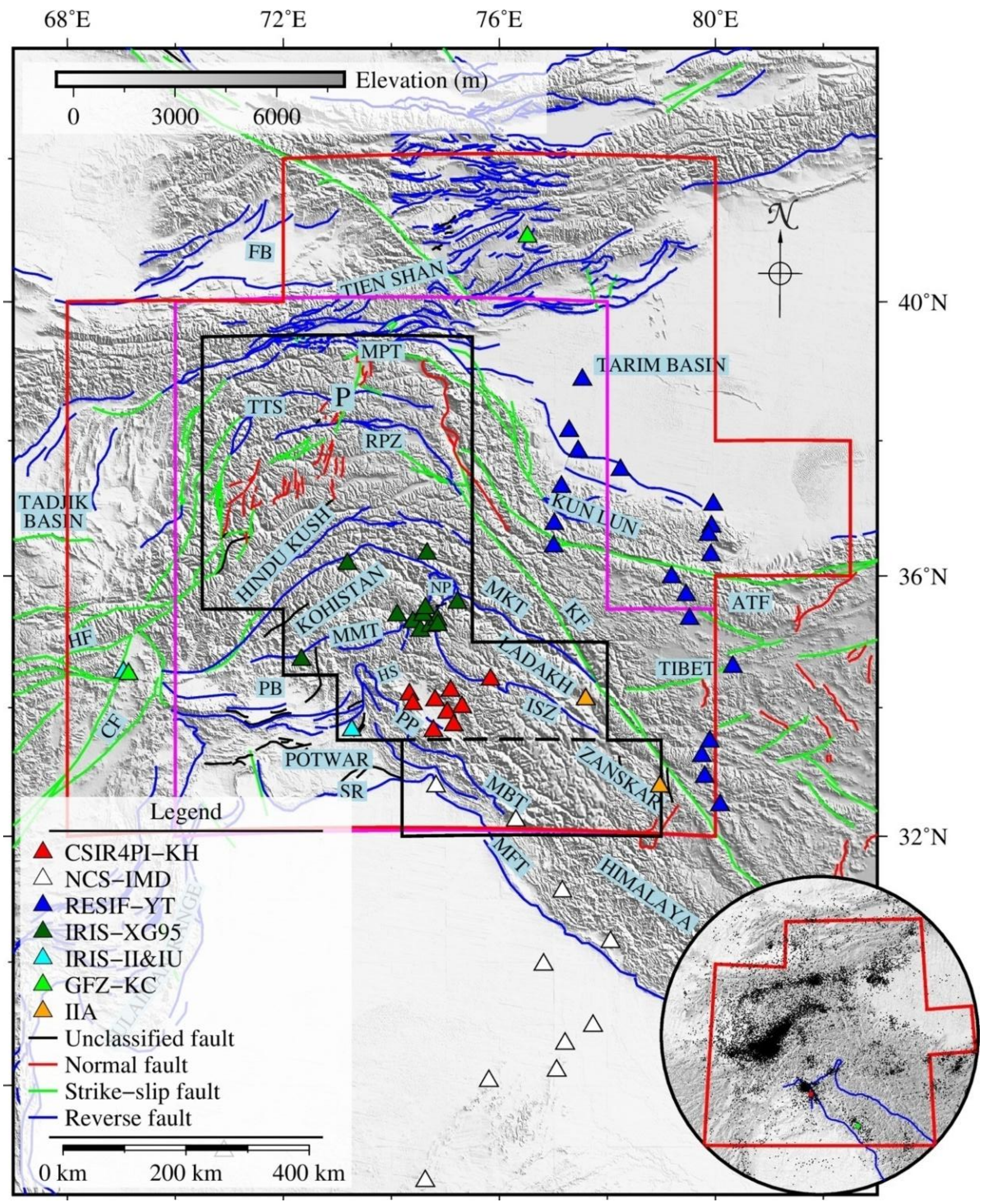

Figure 1, Shows the location of broadband stations used in this study. Red triangles denoted by CSIR4PI-KH (see legend) are Kashmir Himalaya broadband stations operated since June 2013 which contribute ~50% of the data used in this study (Figure A1). Remaining data are from the stations operated by the Indian National Centre for Seismology (NCS), the Incorporated Research Institutions for Seismology (IRIS), the GEOFON stations of German Research Centre for Geosciences (GFZ) and the French Seismologic and Geodetic Network (RESIF). Fault locations were taken from the Central-Asia Fault Database (Mohajder et al. 2016) and Yin (2006) with major tectonic blocks designated after Searle et al. (2001). The Karakoram Fault is denoted by KF, the Main Karakorum Thrust by MKT, and the Indus-Tsangpo Suture by ISZ in Ladakh and the Main Mantle Thrust (MMT) further westward. Other abbreviations are MFT: Main Frontal Thrust, MBT: Main Boundary Thrust, PP: Pir Panjal range SW of the Kashmir basin, ATF: AltynTagh Fault, SR: Salt Range, HS: Hazara Syntaxis, NP: Nanga Parbat syntaxis, CF: Chaman Fault, HF: Heart Fault. The Pamirs (denoted by P) lying between the north bounding Main Pamir Thrust (MPT) and Hindu Kush are divided into 3 main segments by the Tanyamas Thrust system (TTS) and the Rushan-Pshart suture zone (RPZ) (Schurr et al. 2014). Topographic data were taken from ETOPO1 (Amante and Eakins, 2009). The red boundary demarcates the well resolved region at potential resolution of 1° up till the 40 sec period and the magenta one up till 60 sec. The region delineated by the black is well resolved at potential resolution of 0.5° till 60 sec period except for the small region below the dashed line which is well resolved at 0.5 resolution only up to 40 seconds. Inset shows the study region overlaid with 19422 M≥4 earthquake epicenters obtained from the International Seismological Centre (ISC,2016) reviewed catalog for the period 1961-2016. Blue lines denote the MMT/ISZ and the MBT. The red and green circles respectively represent epicenters of 2005 (M_w7.6) Kashmir and 1905 Kangra (M_w7.8; Ambraseys and Douglas, 2004) earthquakes. Note the line of earthquakes marking the Hazara-Nanga Parbat syntaxes (for details see section 4.2).

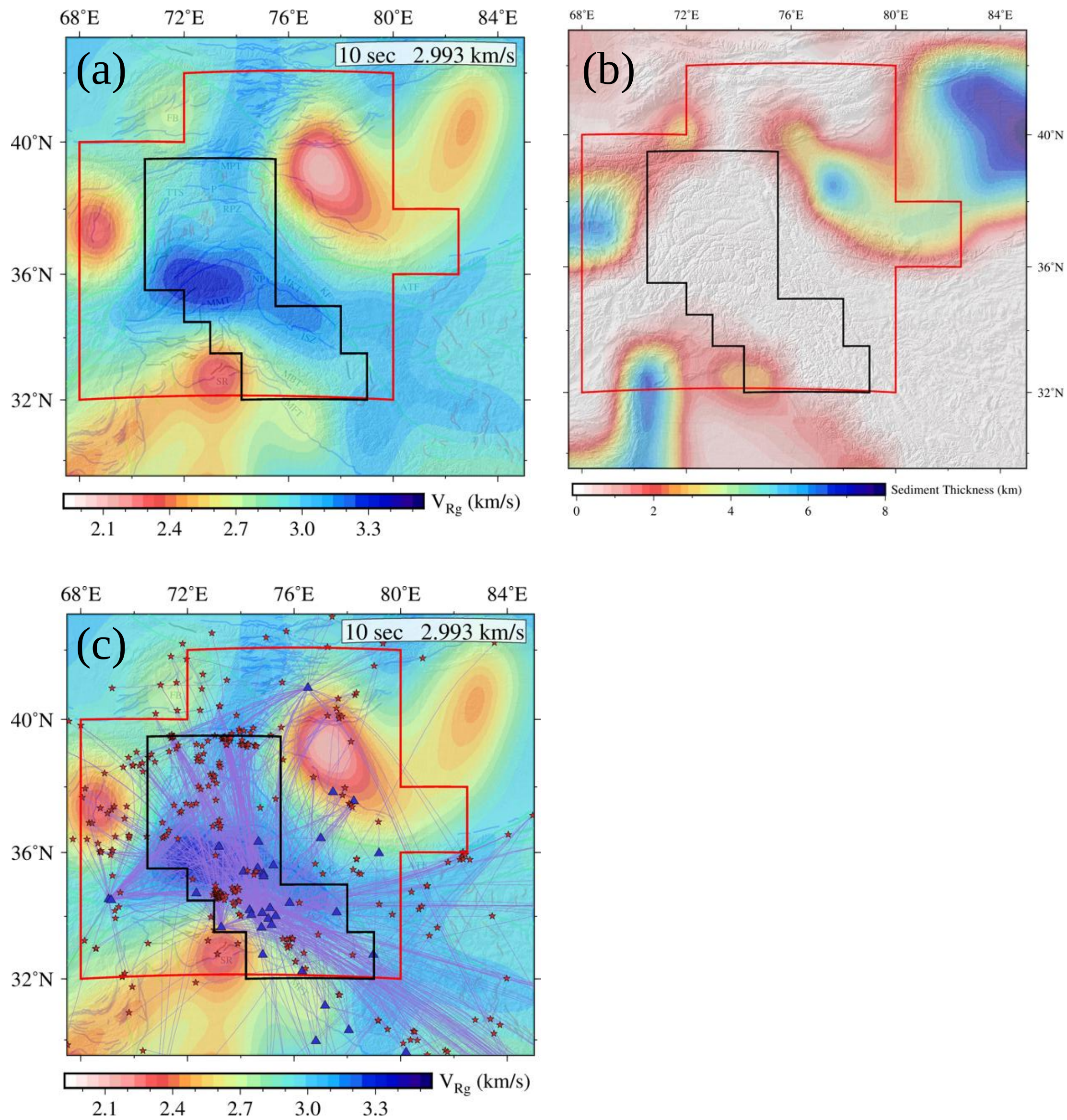

Figure 2, a) shows the 10 sec dispersion map of the region and b) the sediment thickness map of *Laske and Masters* (1997), with boundaries identical to those in Figure 1. The background velocity at this period (2.993 km/s) is shown on the top right of (a). Note the low velocity enclaves corresponding to the prominent sedimentary basins: the Tarim, the Tadjik, the Fergana as well as the Potwar and the Himalayan foreland basin to its southeast; (c) shows great-circle paths between sources (stars) and receivers (triangles) for the 10 second period superimposed on

the group velocity map. Note the high density path coverage over the well resolved region (black boundary) which covers the NW Himalaya, the Hindu Kush and the Pamir. The larger region marked by the red boundary is well resolved at lesser resolution. High velocity signature of the Aravalli craton can also be seen at this period (Figure A2) even as it lies far outside the red boundary, testifying to the robustness of dispersion maps.

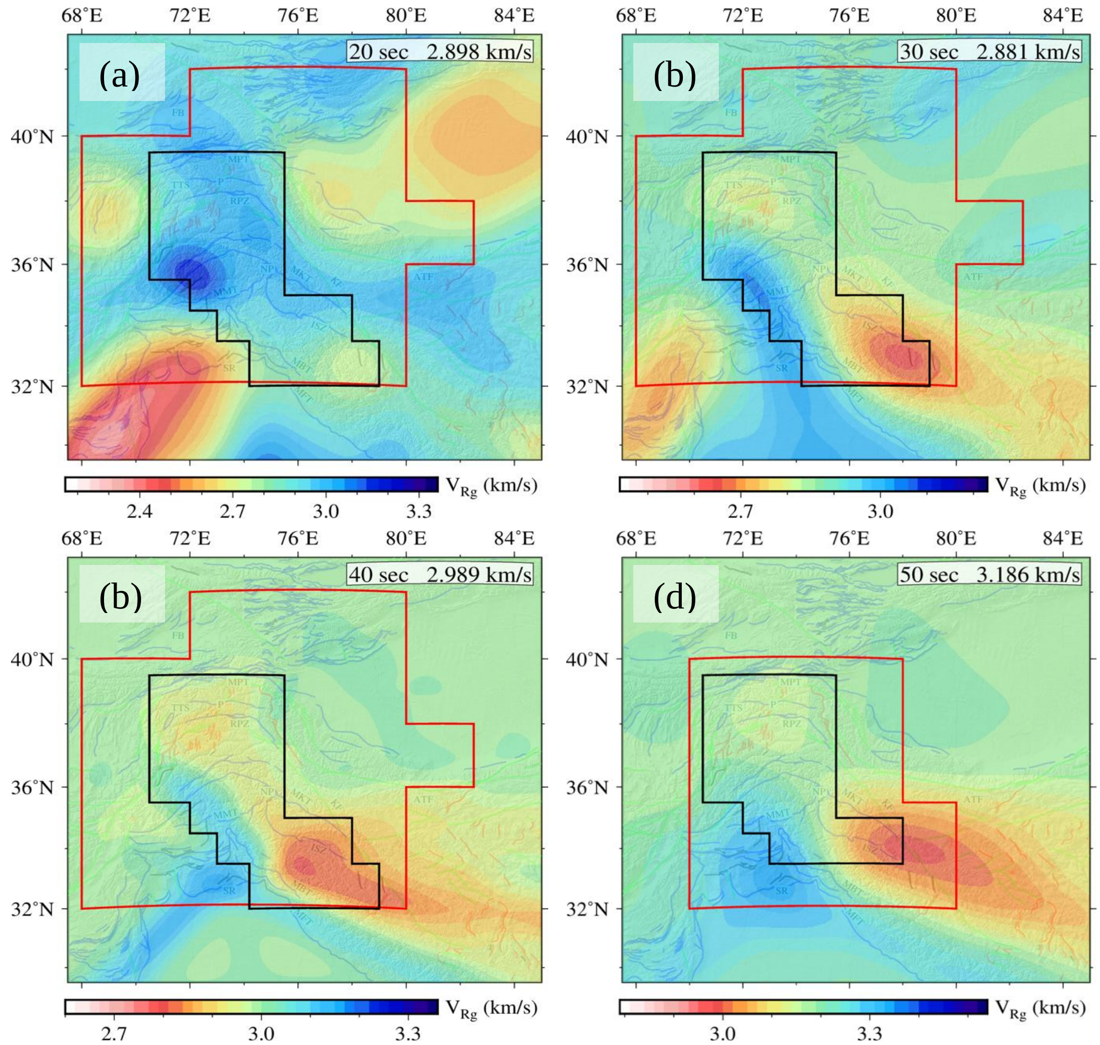

Figure 3 shows fundamental mode Rayleigh wavegroup velocity maps for periods of 20, 30, 40, and 50 sec, with background velocities at each period shown on the top right. Low velocity signatures of the Tadjik, the northern Indus and the western Tarim basins are seen even on the 20 sec period map. The prominent high velocity cores of the Hindu Kush and Nanga Parbat persists up to ~30 sec period, merging with that representing the Indian plate at higher periods. Low velocities beneath southwestern Tibet, Zanskar and the Ladakh Himalaya, for periods higher than 20 s, reflect the thicker crust underneath. The regions within the various colored polygons have resolutions as stated in the caption of Figure 1.

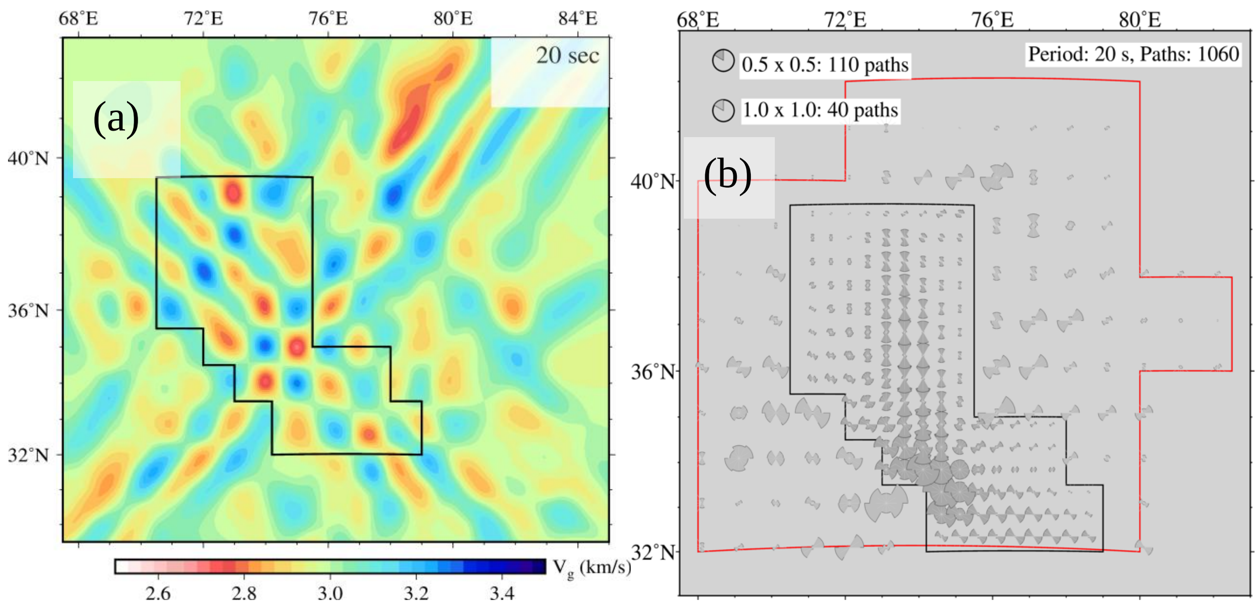

Figure 4, (a) shows checkerboard solution model for 0.5° × 0.5° anomalies with the maximum available raypath coverage at the 20 s period. Note that NW Himalaya and the adjoining regions of Kohistan, Hindu Kush, and Pamir are well resolved (b) shows azimuthal variation and path density of rays at 0.5° × 0.5° grid nodes for the region bounded by the black polygon and at 1.0° × 1.0° for the surrounding area bounded by the red polygon. Scales representing number of paths for the two regions are stated on the left hand top corner.

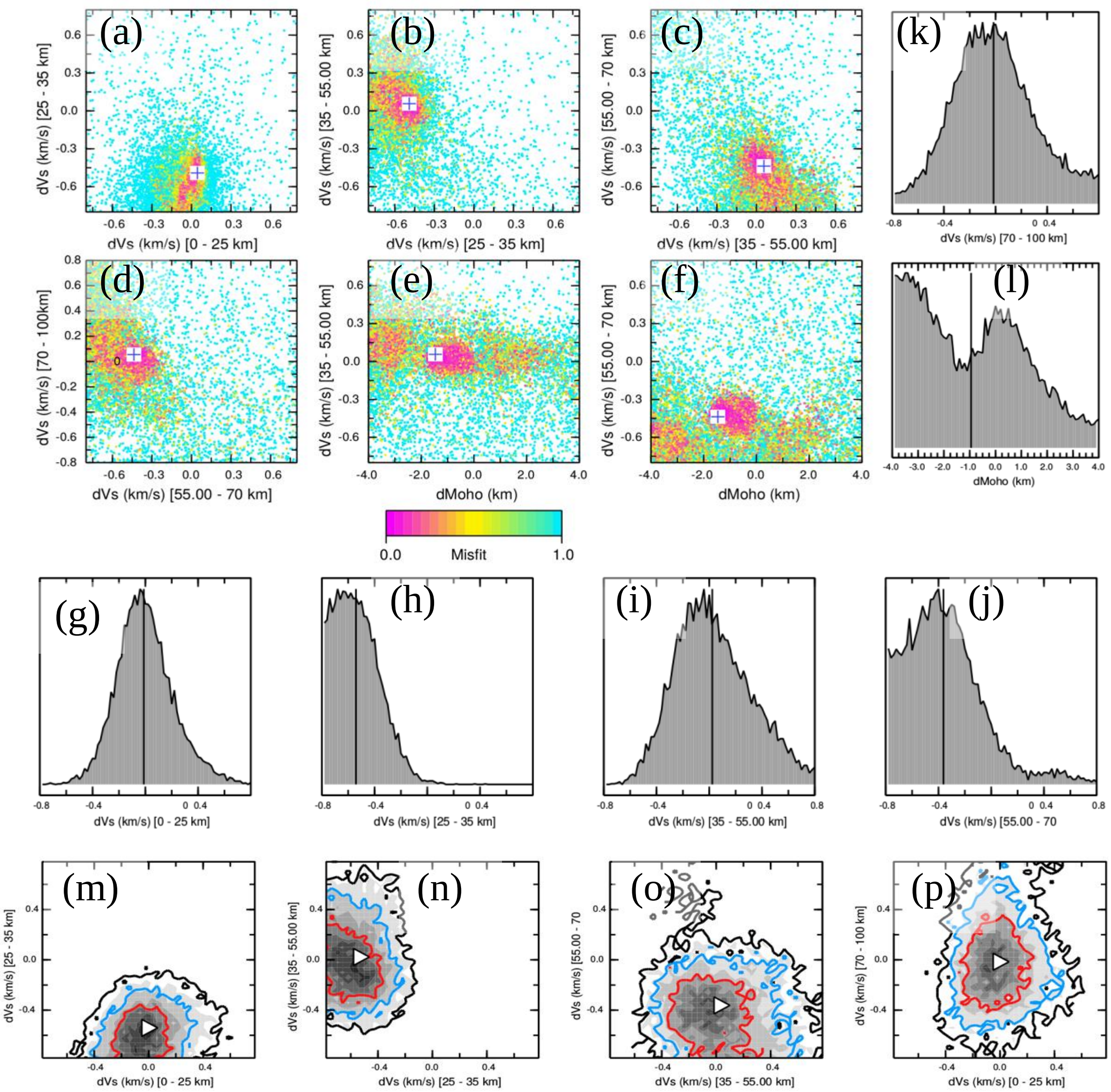

Figure 5(a-f) shows the models (32200) generated for the site 34.5N, 74.5E using NA sampling, by perturbing the a-priori model for the same site taken from *Maurya et al.* (2016).The dense regions with '+' sign show the models with least misfit. The a-priori Moho depth beneath this site was 55km at which Vs crosses the 4.4km/s value. Note the close-fitting convergence regions upto Moho (a-c), even as the convergence of Vs is not global for the upper mantle. (g-l) shows the 1D Posterior Probability Distribution Functions (PPDF) for Vs from 0-100 km and the Moho depth (55 km), the x-axis denoting allowed deviations of the parameter(±0.8 km/s for Vs and ±4

km for the Moho) and the y-axis, its probability. Note that Vs is well resolved till 100 km (g-k), while the Moho depth is less well resolved (l). The black line denotes the posterior mean of the parameter e.g. [$V_{s(55\text{-}70)}$- 0.39] km/s for the 55-70 km layer shown in (j)]. (m-p) showthe 2-D PPDF’s for Vs up till 100 km, where 90% confidence intervals are shown in red, and the triangles denote its posterior mean values.

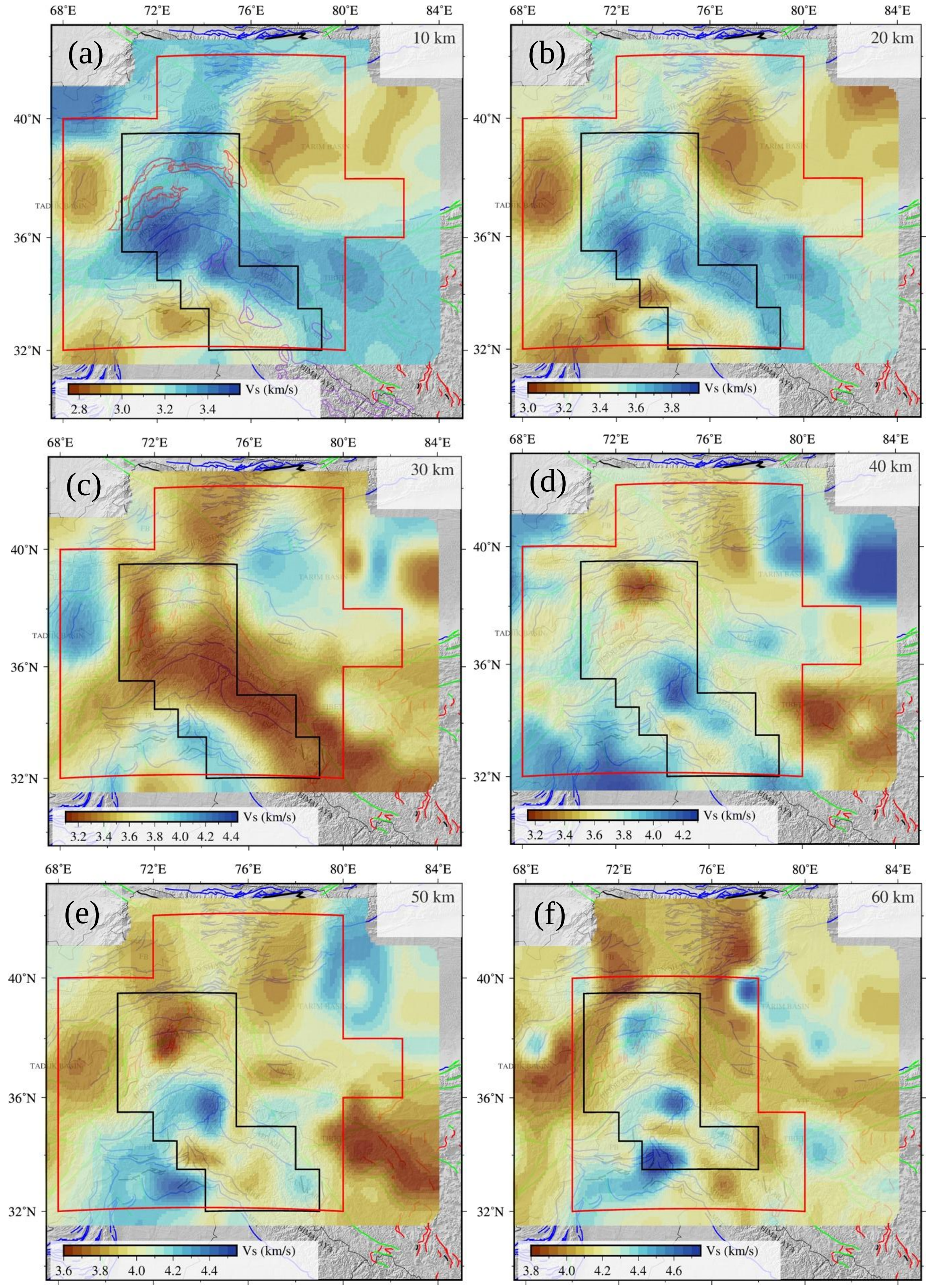

(a)
10 km
Vs (km/s)
2.8 3.0 3.2 3.4
(b)
20 km
Vs (km/s)
3.0 3.2 3.4 3.6 3.8
(c)
30 km
Vs (km/s)
3.2 3.4 3.6 3.8 4.0 4.2 4.4
(d)
40 km
Vs (km/s)
3.2 3.4 3.6 3.8 4.0 4.2
(e)
50 km
Vs (km/s)
3.6 3.8 4.0 4.2 4.4
(f)
60 km
Vs (km/s)
3.8 4.0 4.2 4.4 4.6
68°E 72°E 76°E 80°E 84°E
40°N 36°N 32°N

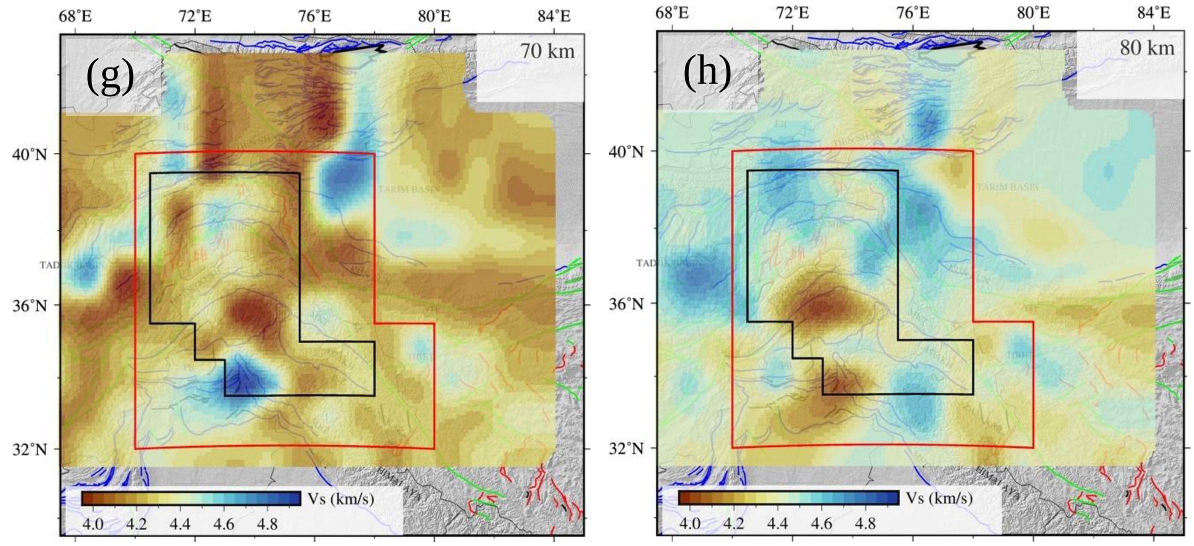

Figure 6 (a-h) shows slices of shear wave velocities in the region between 10-80 km, at depth intervals of 10 km. Note the high velocity enclaves beneath the Pamir, the Nanga Parbat and the Ladakh Himalaya at 10 km depth, becoming stronger at 20 km depth. These correlate well with surface exposures of the gneiss domes in Pamir and with the crystalline complexes beneath the Nanga Parbat (drawn in a). Also note the low velocity layer beneath the Himalaya, Tibet, Hindu Kush at depth of 30 km (c), with Pamir at a marginally higher velocity of ~3.7 km/s. For details see sections 3 and 4. Posterior error map for each slice (a-h) is plotted in Figure A3. The regions within the various colored polygons have resolutions as stated in the caption of Figure 1.

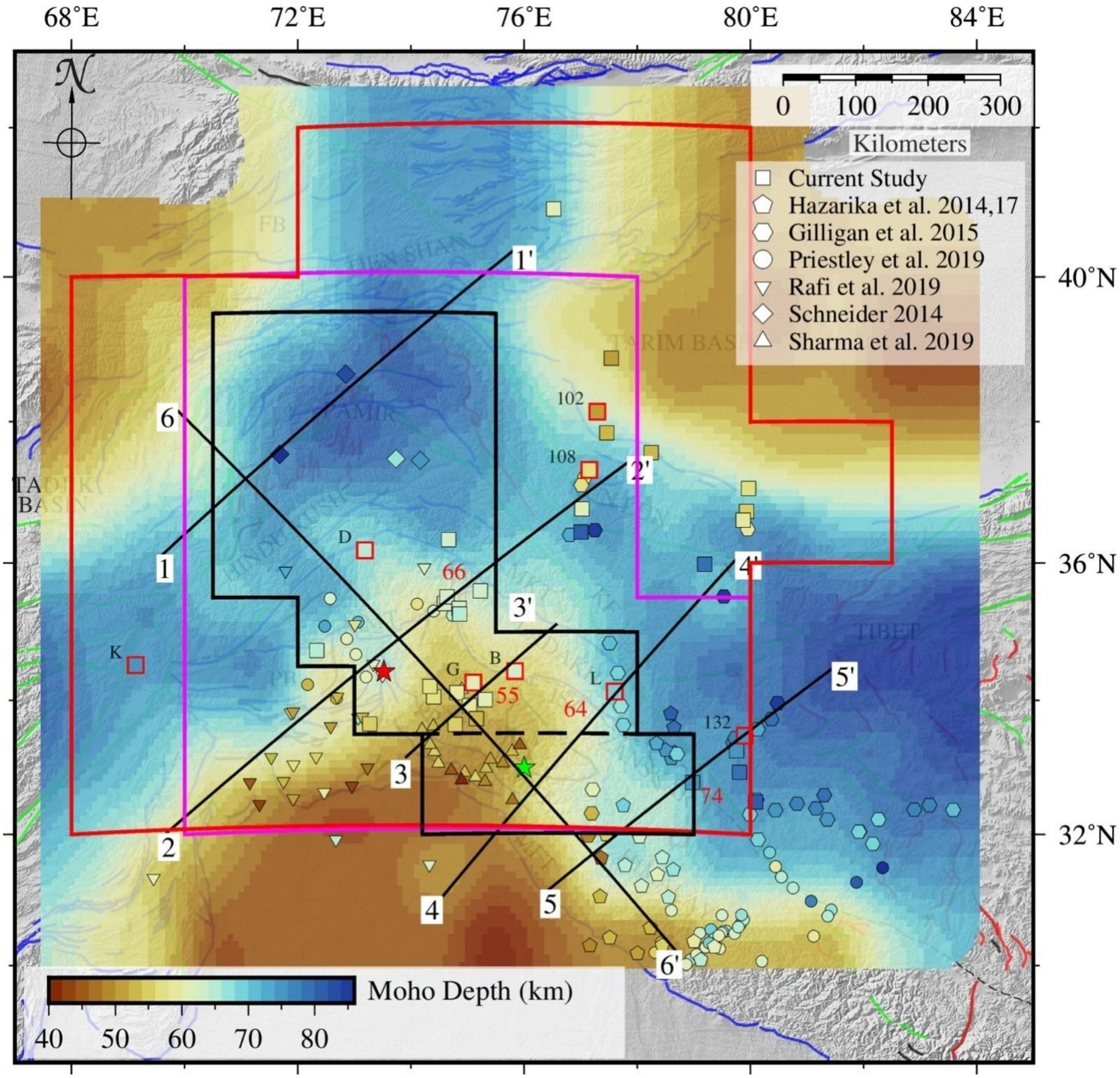

Figure 7 shows posterior Moho depth estimates for the region. The a priori Moho was chosen as the depth where Vs crosses the iconic value of 4.4 km/s. The average Moho depth in the region is found to be ~70 km, with higher depths beneath Tibet and the Pamir and shallow beneath the Tarim, Tadjik and Fergana basins, as well as theHimalayan foreland basin. Moho depths calculated from joint inversion of RFs and surface wave dispersion data at 38 sites are shown as squares on this map using the same color code as those used for the NA inversions (see legend).

All authors mentioned in the legend have used either RF inversion or joint inversion of RF and surface wave data to constraint the Moho depths underneath, except Schneider (2014) who used a slant-stacking method. The Moho is found to be distinctly shallower by as much as 10 km in the region bounded by arc-normals that pass through the epicenters of the 1905 Kangra and 2005 Kashmir earthquakes marked as green and red stars respectively (ISC, 2016; Ambrayses and Doughlas, 2004). Estimated Moho depths within the black region are largely consistent with published results. A notable feature of this map is the continuance of deeper Moho further northeast of the Kunlun-AltynTagh fault compared with estimates reported earlier (e.g. Wittlinger et al., 2004). Velocity structure beneath 8 of the 38 sites marked with red boundary and denoted by the first letter of their station code (full name if numeric) is shown in Figure 8. The posterior shear-wave velocity structure with depth along 5 NE-SW profiles, labeledas1-1' to 5-5' are shown in Figure 9, along with a NW-SE profile 6-6'. The regions within the various colored polygons have resolutions as stated in the caption of Figure 1.

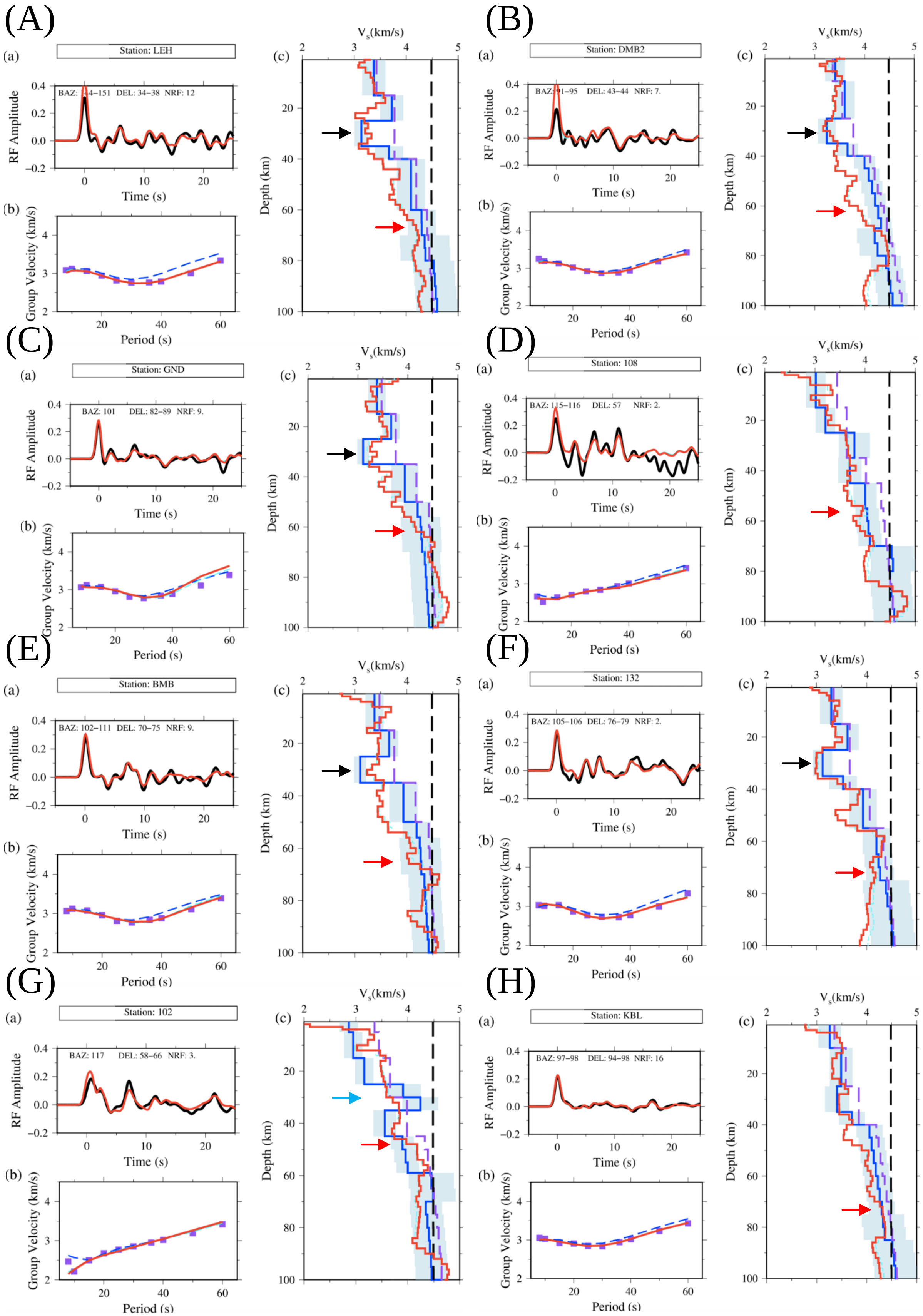
(A)
(a)
Station: LEH
DEL: 34–38 NRF: 12
RF Amplitude
Time (s)
(b)
Group Velocity (km/s)
Period (s)
(c)
V_s(km/s)
Depth (km)
(B)
Station: DMB2
DEL: 43–44 NRF: 7.
(C)
Station: GND
BAZ: 101 DEL: 82–89 NRF: 9.
(D)
Station: 108
BAZ: 115–116 DEL: 57 NRF: 2.
(E)
Station: BMB
BAZ: 102–111 DEL: 70–75 NRF: 9.
(F)
Station: 132
BAZ: 105–106 DEL: 76–79 NRF: 2.
(G)
Station: 102
BAZ: 117 DEL: 58–66 NRF: 3.
(H)
Station: KBL
BAZ: 97–98 DEL: 94–98 NRF: 16

Figure 8 shows the posterior shear wave velocity models (blue lines), overlaid on models obtained from joint inversion of receiver function and weakly weighted (10 and 20%) surface wave dispersion measurements (red & cyan lines) for 8 different sites (A-H). Locations of sites are shown in Figure 7 as squares within the red boundary. At each site, the station name is plotted on top of the calculated (black) and recovered receiver functions (red), plotted in (a). Observed (purple) and predicted (blue, red and cyan) dispersion curves are plotted in (b). The a-priori Vs model from Maurya et al. (2016) is plotted as a dashed purple line in (c) along with the posterior Vs model (blue) where the error bounds on Vs (light blue) represent the mean error of the ensemble of best models. The initial model for joint inversion is shown by the black dashed line (Vs ~4.48 km/s) and the corresponding final model, by red and cyan lines, respectively representing 10% and 20% weightage of surface waves dispersion data in joint inversion. Note the appearance of the pervasive low velocity layer at depths of ~25-35 km, except at the stations 102, 108 and KBL.Moho depths are denoted by red arrows and the intra crustal low velocity layer at ~30 km, observed at few stations (B,C,E,F), by black arrows. A high velocity layer observed at ~30 km beneath the Tarim basin (G) is marked by a blue arrow.

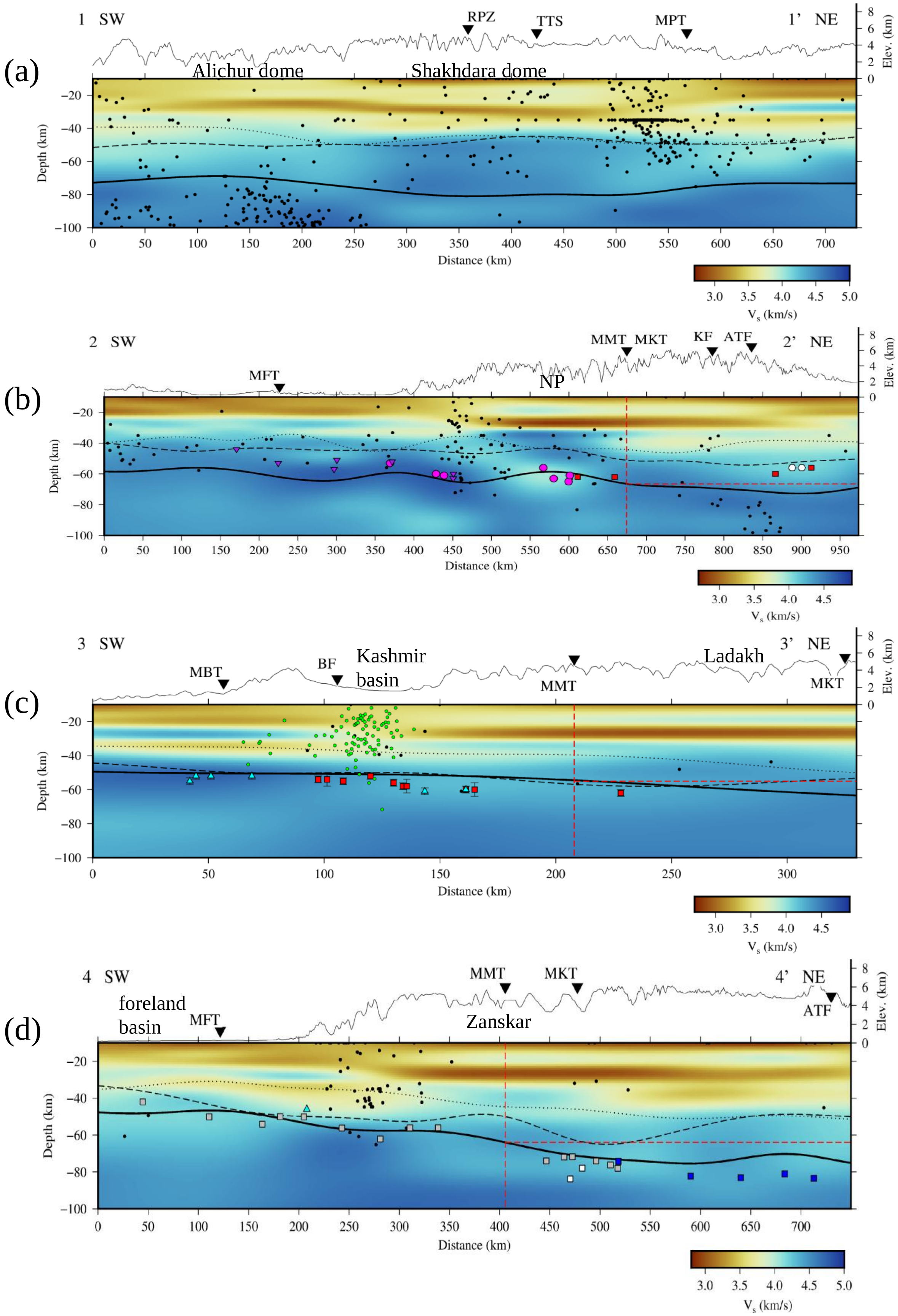

(a)
1 SW
RPZ
TTS
MPT
1' NE
Alichur dome
Shakhdara dome
Elev. (km)
Depth (km)
Distance (km)
Vs (km/s)
(b)
2 SW
MFT
NP
MMT MKT
KF ATF
2' NE
Elev. (km)
Depth (km)
Distance (km)
Vs (km/s)
(c)
3 SW
MBT
BF
Kashmir basin
MMT
Ladakh
3' NE
MKT
Elev. (km)
Depth (km)
Distance (km)
Vs (km/s)
(d)
4 SW
foreland basin
MFT
MMT
MKT
Zanskar
4' NE
ATF
Elev. (km)
Depth (km)
Distance (km)
Vs (km/s)

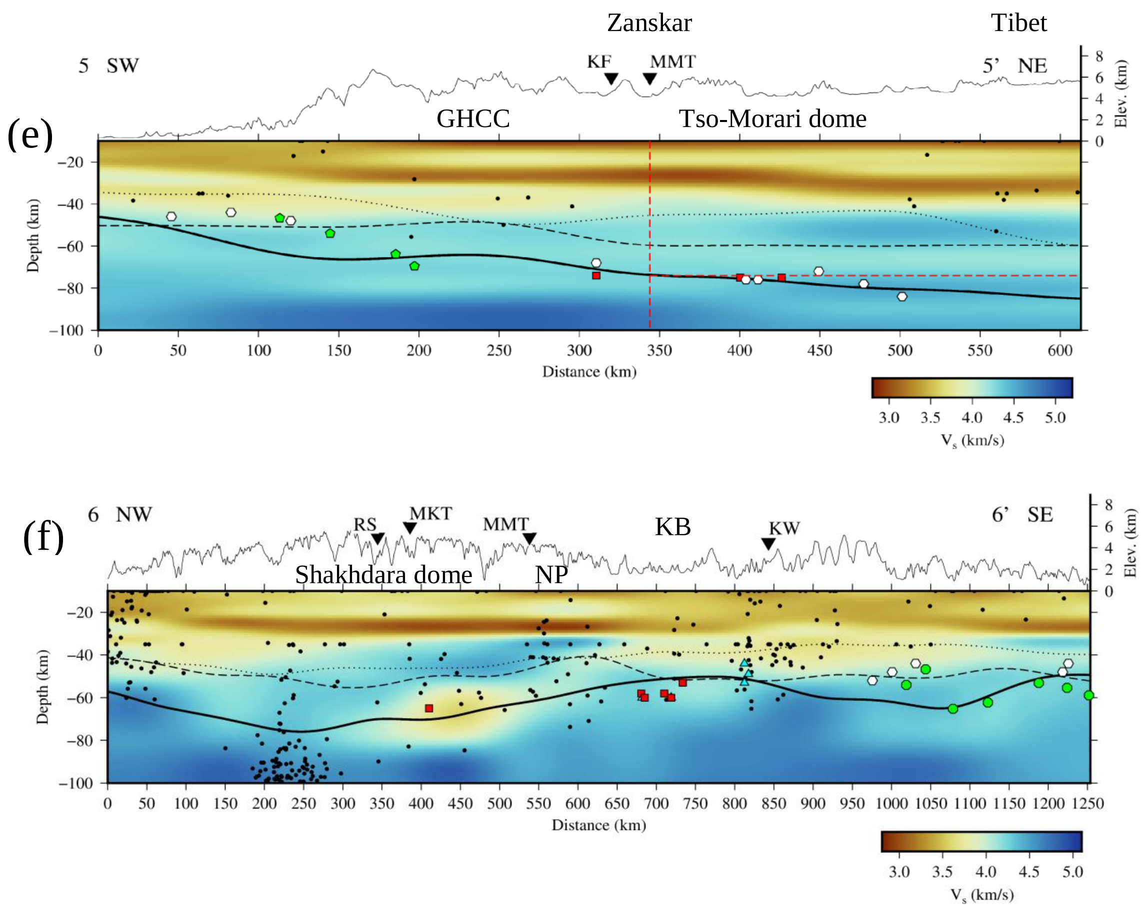

Figure 9, shows the posterior Vs cross-sections and Moho depths along 5 NE-SW (a-e) and 1 NW-SE profile (f), marked by dotted, dashed and solid black lines, respectively estimated from 3 different initial a-priori models identifying the Moho surface with velocities of 4.0, 4.2 and 4.4 km/s. Moho surfaces for depths marked on each profile are values constrained by inversions of receiver functions (Figure 7), some jointly with surface wave dispersion data, and no farther than 35 km from it to ensure consistency with the lateral resolution of receiver function. Profile (a)which crosses2 of the 5 gneiss domes in Pamir including the largest Shakhdara dome are clearly identified by their high velocity signatures up to ~20 km. Similarly, profile (b) which

extends from the foreland basin in the southwest to Nanga Parbat (NP) also brings out the high velocity character of the latter. Note also that Moho depth beneath the MMT north of the NP is 66.5 km, marked by a dashed red line. Profiles (c) and (d) shows Moho depths and Vs along two profiles [Mir et al. unpublished (c); *Rai et al.* 2006 (d)], indicating that Moho depths beneath the MMT southeastwards are 55 km and 64 km respectively.The easternmost arc-normal profile (e) passing through Shimla and the Ladakh Himalaya, shows shallow high V_s velocities corresponding to the surface location of the Greater Himalayan Crystalline complexes (GHCC) and the Tso-Morari gneiss dome. The corresponding Moho depth beneath the MMT is ~74 km, confirming that the Moho is shallower by ~10 km beneath the NW Himalaya. The NW-SE profile (f) passes from Pamir to Kishtwar (KW), through Hindu-Kushand the Kashmir Basin (KB), shows that the deepest Moho lies beneath the Pamir and the Hindu Kush. However, the pervasive low velocity layer at ~30 km found throughout the Himalayas is notably absent beneath the Kashmir basin.

References

Acton, C.E., Priestley, K., Gaur, V.K., Rai, S.S., 2010. Group velocity tomography of the Indo–Eurasian collision zone. J. Geophys. Res. 115, B12335.

Amante, C. and B.W. Eakins, 2009. ETOPO1 1 Arc-Minute Global Relief Model: Procedures, Data Sources and Analysis. NOAA Technical Memorandum NESDIS NGDC-24. National Geophysical Data Center, NOAA. doi:10.7289/V5C8276M

Ambraseys, N. and J. Douglas, (2004). Magnitude calibration of north Indian earthquakes. Geophys. J. Int., 159:165–206.

Beyreuther, M., Barsch, R., Krischer, L., Megies, T., Behr, Y., and Wassermann, J. (2010), ObsPy: A Python Toolbox for Seismology, *Seis. Res. Lett.*, 81 (3), 530-533.

Dziewonski, A., Bloch, S. and Landisman, M., 1969. A technique for the analysis of transient seismic signals, *Bull. Seism. Soc. Am.*, 59, 427– 444.Laske G. and G. Masters, A Global Digital Map of Sediment Thickness, *EOS Trans.* AGU, 78, F483, 1997.

Gilligan, A., Priestley, K. F., Roecker, S. W., Levin, V., Rai, S., (2015). The crustal structure of the western Himalayas and Tibet. J.Geoph. Res.: Solid Earth Earth 120 (5), 3946–3964.

Gilligan, A., and Priestley, K. (2018). Lateral variations in the crustal structure of the Indo-Eurasian collision zone. *Geophy. J. Int.*, *214*(2), 975-989. DOI: 10.1093/gji/ggy172

Goldstein, P., and A. Snoke (2005). SAC Availability for the IRIS Community, Incorporated Research Institutions for Seismology Data Management Center, Electronic Newsletter, available at http://ds.iris.edu/ds/newsletter/vol7/no1/sac‐availability‐for‐the‐iris‐community/(last accessed January 2013).

Guo, Z., X. Gao, H. Yao, J. Li, and W. Wang (2009), Midcrustal low-velocity layer beneath the central Himalaya and southern Tibet revealed by ambient noise array tomography, *Geochem. Geophys. Geosyst.*, 10, Q05007, doi:10.1029/2009GC002458.

Hazarika D., Sen K., Kumar N. (2014). Characterizing the intracrustal low velocity zone beneath northwest India–Asia collision zone, Geophy. J. Int., 99, 3, 1338–1353, https://doi.org/10.1093/gji/ggu328

Hazarika, D., Wadhawan, M., Paul, A., Kumar, N., Borah, K., 2017. Geometry of the Main Himalayan Thrust and Moho beneath Satluj Valley, northwest Himalaya: Constraints from receiver function analysis. J.Geoph. Res.: Solid Earth 122 (4), 2929–2945.

Herrmann, R.B., 1973. Some aspects of band-pass filtering of surface waves, *Bull. seism. Soc. Am.*, 63, 663–671.

Herrmann, R.B. and Ammon, C.J., 2004. Surface waves, receiver functions and crustal structure, in Computer Programs in Seismology, Version 3.30, Saint Louis University, http://www.eas.slu.edu/People/RBHerrmann/CPS330.html

International Seismological Centre, On-line Bulletin, http://www.isc.ac.uk, Internatl. Seismol. Cent., Thatcham, United Kingdom, 2016. http://doi.org/10.31905/D808B830

Jade, S., Mir, R.R., Vivek, C.G. et al. Crustal deformation rates in Kashmir valley and adjoining regions from continuous GPS measurements from 2008 to 2019. *Sci Rep* 10, 17927 (2020). https://doi.org/10.1038/s41598-020-74776-5

Kumar S. Magnetic Susceptibility Mapping of Ladakh Granitoids, northwest higher Himalaya: Implication to redox series of felsic magmatism in the subduction environments (2008), Mem. Geol.. Soc. India (BR Arora and R. Sharma, Eds.), 72, 83-102

Laske, G. and Masters, G., 1997. A global digital map of sediment thickness,*EOS, Trans. Am. geophys. Un.*, 78, F483.

Laske, G., Masters., G., Ma, Z. and Pasyanos, M., Update on CRUST1.0 - A 1-degree Global Model of Earth's Crust, *Geophys. Res. Abstracts*, 15, Abstract EGU2013-2658, 2013.

Li W., Chen Y., Yuan X.,SchurrB., Mechie J.,OimahmadovI.,and Fu B., (2018) Continental lithospheric subduction and intermediate-depth seismicity: Constraints from S-wave velocity structures in the Pamir and Hindu Kush, *Earth Planet. Sci. Lett., 482, 478–489*

Maurya, S., J.-P. Montagner, M. R. Kumar, E. Stutzmann, S. Kiselev, G. Burgos, N. P. Rao, and D. Srinagesh (2016), Imaging the lithospheric structure beneath the Indian continent, *J. Geophys. Res.* Solid Earth, 121, doi:10.1002/2016JB012948.

Mir R. R., Parvez I. A., Gaur V. K., Chandra R., Romshoo S. A., (2017) Crustal structure beneath the Kashmir Basin adjoining the western Himalayan syntaxis. *Bull.Seismol. Soc. Am.* 107(5):2443–2458

Mitra, S., K. Priestley, V. Gaur, S. Rai, and J. Haines (2006), Variation of Rayleigh wave group velocity dispersion and seismic heterogeneity of the Indian crust and uppermost mantle, *Geophys. J. Int.*, 164(1), 88–98.

Mohadjer, S., Ehlers, T.A., Bendick, R., Stübner, K., Strube, T. (2016) A Quaternary fault database for central Asia, Nat. Hazards Earth Syst. Sci., 16, 529-542, doi:10.5194/nhess-16-529-2016.

Okabe, A., Boots B., Sugihara K., Chiu S. N., (2000). Spatial Tessellations: Concepts and Applications of Voronoi Diagrams, 2nd Edition, Wiley, pp. 696

Park, S., and Mackie, R., (1997). Crustal structure at Nanga Parbat, northern Pakistan, from magnetotelluric soundings, Geophy. Res. Lett., 24, 2415-2418.

Priestley K., Ho T., and Mitra S., (2019). The crust structure of the Himalaya: a synthesis, Geological Society, London, Special Publications, 483, https://doi.org/10.1144/SP483-2018-127

Rafi, Z., Priestley, K., Mahmood, N., Gilligan, A., 2019. Crustal structure of the Indus Valley Plain and the Western Himalayan Syntaxis of Pakistan. Geophysical Journal International submitted.

Rai, S.S., Priestley, K., Gaur, V.K., Mitra, S., Singh, M.P. & Searle, M., 2006. Configuration of the Indian Moho beneath the NW Himalaya and Ladakh, Geophys. Res. Lett., 33, L15308, doi:10.1029/2006GL026076.

Rawlinson, N., Sambridge, M., 2004. Wavefront evolution in strongly heterogeneous layered media using the fast marching method. Geophys. J. Int. 156, 631–647.

Rawlinson, N. and Sambridge M., 2005. The fast marching method: An effective tool for tomographic imaging and tracking multiple phases in complex layered media,*Explor. Geophys.*, 36, 341-350

Ritzwoller, M. H., Shapiro, N. M., Barmin, M. P., &Levshin, A. L., 2002. Global surface wave diffraction tomography, *J. Geophys. Res.*: Solid Earth, 107(B12)

Sambridge, M., Geophysical Inversion with a Neighbourhood Algorithm -I. Searching a parameter space, Geophys. J. Int., 138 , 479-494, 1999a.

Sambridge, M., Geophysical Inversion with a Neighbourhood Algorithm -II. Appraising the ensemble, Geophys. J. Int., 138 ,727-746, 1999b.

Schiffman, C., B. S. Bali, W. Szeliga, and R. Bilham (2013). Seismic slip deficit in the Kashmir Himalaya from GPS observations, Geophys. Res. Lett. 40, 5642–5645, doi: 10.1002/2013GL057700.

Schneider, F. (2014), Imaging an Intra-continental Subduction in Central Asia with Teleseismic Receiver Functions. Scientific Technical Report 14/06, GFZ German Research Centre for Geosciences. doi: 10.2312/GFZ.b103-14063

SchneiderD. A., M. A. Edwards, W. S. F. Kidd, M. Asif Khan, L. Seeber, P. K. Zeitler; Tectonics of Nanga Parbat, western Himalaya: Synkinematic plutonism within the doubly vergent shear zones of a crustal-scale pop-up structure. (1999) Geology ; 27 (11): 999–1002

Schurr, B., Ratschbacher, L., Sippl, C., Gloaguen, R., Yuan, X., Mechie, J., 2014. Seis-motectonics of the Pamir. Tectonics 33, 1501–1518. http://dx.doi.org/10.1002/ 2014TC003576

Searle, M., Hacker, B. R., and Bilham R., (2001). The Hindu Kush Seismic Zone as a Paradigm for the Creation of Ultrahigh-Pressure Diamond- and Coesite-Bearing Continental Rocks, *The Journal of Geology*, 109, 143–153

Sharma, S., Mitra, S., Priestley, K., Powali, D., Wanchoo, S., 2019. Crustal structure of the Jammu and Kashmir Himalayas. Geophy. J. Int. submitted.

Wessel, P., W. H. F. Smith, R. Scharroo, J. F. Luis, and F. Wobbe (2013). Generic Mapping Tools: Improved version released, Eos Trans. AGU 94, 409–410

Wittlinger, G., Vergne, J., Tapponnier, P., Farra, V., Poupinet, G., Jiang, M., et al. (2004). Teleseismic imaging of subducting lithosphere and Moho offsets beneath western Tibet. *Earth and Planet. Sc. Lett.*, 221(1), 117–130.

Yao, H., Beghein, C., Van Der Hilst, R. D., 2008. Surface wave array tomography in SE Tibet from ambient seismic noise and two-station analysis - II. Crustal and upper-mantle structure. *Geophy, J. Int.* 173(1): 205-219.

Yin, A., (2006).Cenozoic tectonic evolution of the Himalayan orogen as constrained by along-strike variation of structural geometry, exhumation history, and foreland sedimentation.Earth Sci. Rev., 76, 1–131.

Appendix

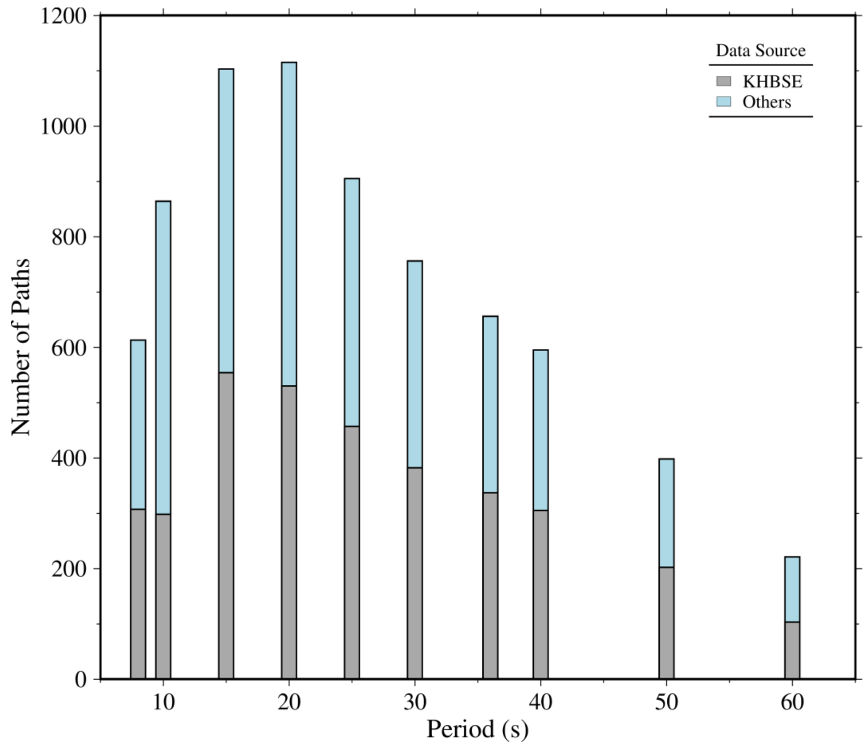

Figure A1: shows the period-dependent availability of data. X-axis denotes the period and y-axis is number of paths. Note that about 50% of the data originates from Kashmir Himalaya broadband seismic experiment (KHBSE).

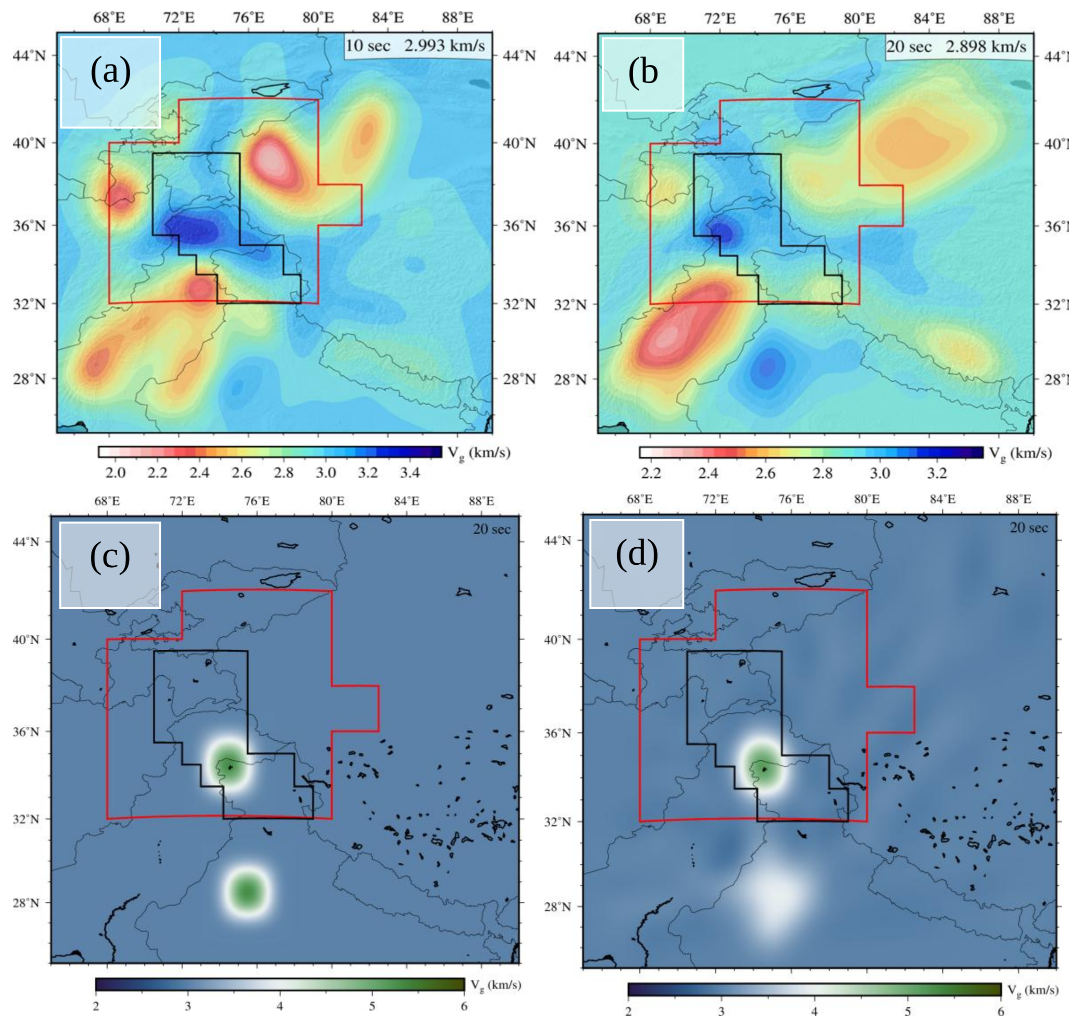

Figure A2 (a) shows fundamental mode Rayleigh wave dispersion map at 10 sec including south of the study region (bounded red polygon). Note a velocity enclave (~3.1 km/s) centred about 28° N and 75.5° E, with a slightly higher velocity (~3.25 km/s) on 20 sec map (b), which geographically coincides with the location of Aravalli craton. To check this possibility, we carried out a spike test. The input model, with a positive spike at this point and an another spike centered NW of Kashmir, in the well resolved area is shown in (c) and (d) shows the corresponding inverted solution. Whilst the recovery of the Aravalli centred spike is only in the form of a diffused halo as expected from its location, its unmistakable identification with the northwestern core of the Aravalli craton at least up to periods of 20 seconds, testifies to the robustness of the dispersion maps.

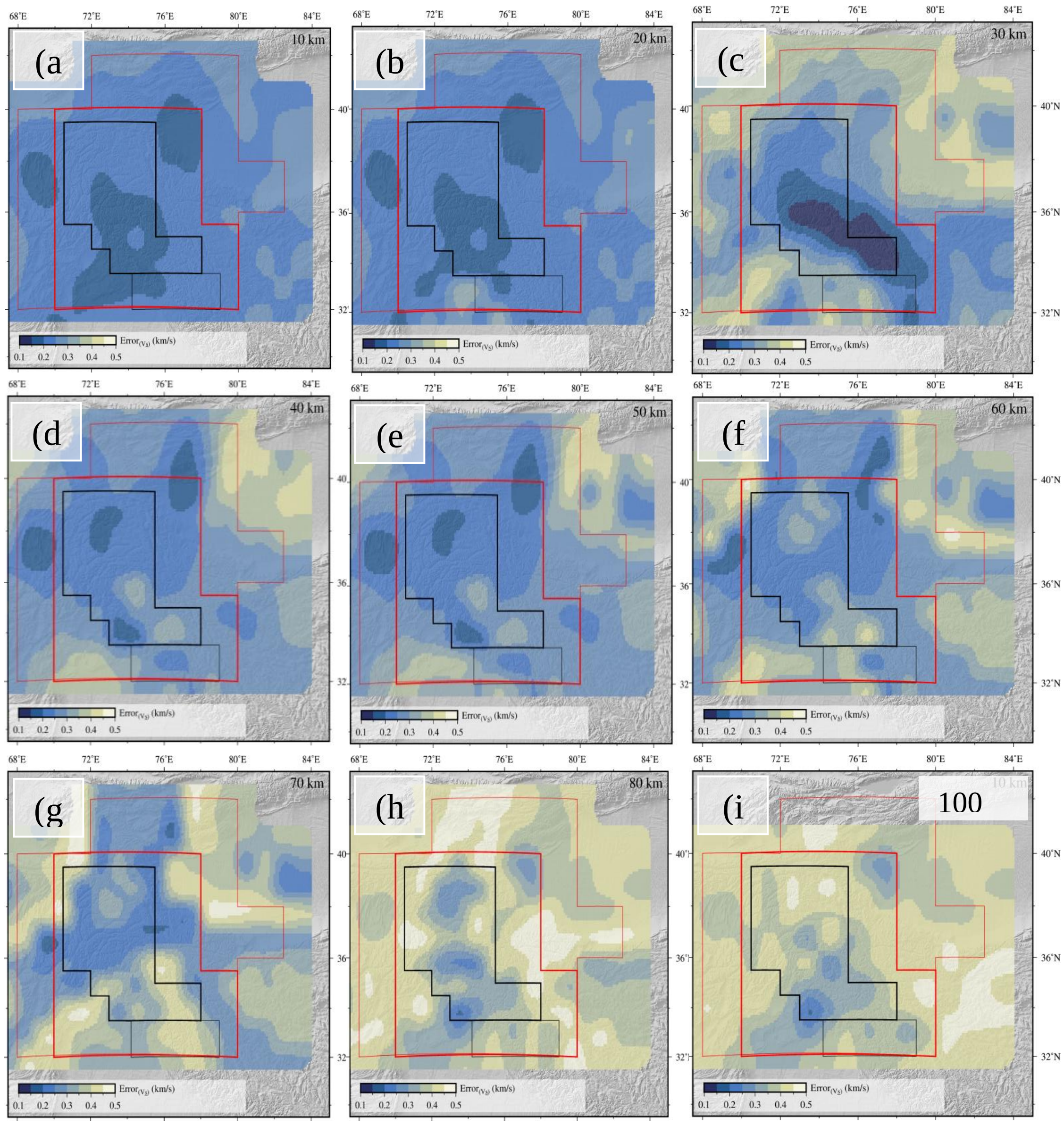

Figure A3: shows posterior Vs errors for shear wave velocity maps shown in Figure 6 of main text. Note the lesser errors (<0.2 km/s) at 30 km depth (c) which corresponds to intra-crustal low velocity layer beneath the NW Himalaya and Hindu Kush.

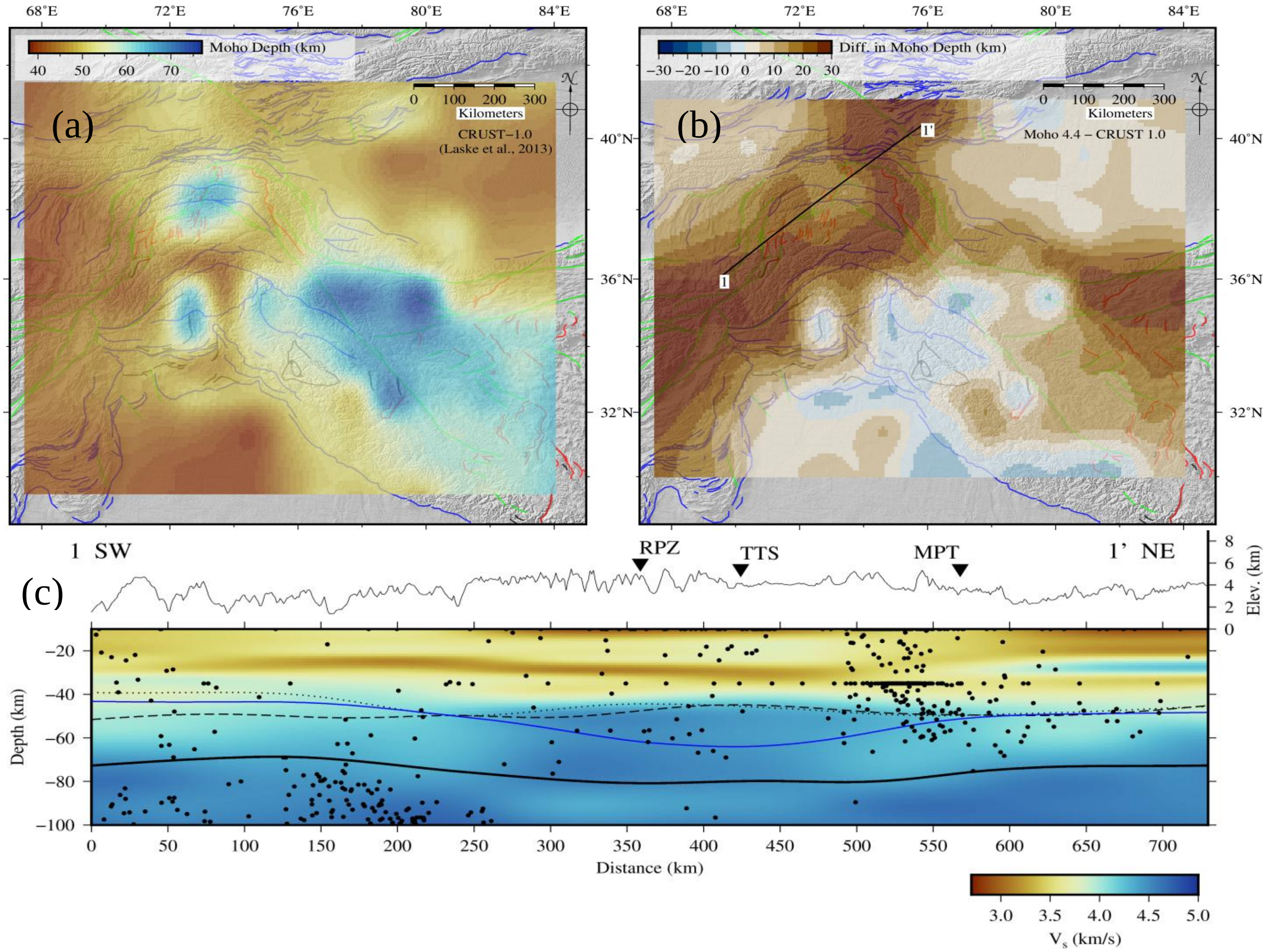

Figure A4: (a) shows Moho depth estimates for the region from global crustal model CRUST 1.0 (Laske et al. 2013). Note the deeper Moho estimates for regions like north-central Pamirs, Hindu Kush and Tibet. (b) shows the Moho difference map produced by subtracting depths given in (a) from posterior Moho estimates obtained in the current study (Figure 7). Except Pamir, Hindu Kush and western Tibet, Moho estimates are within 10 km. (c) shows Vs cross-section along profile 1-1' (same as Figure 9a of main text) with Moho from CRUST 1.0 marked as blue line. Schneider (2014) has reported deeper Moho (up to 85 km) beneath the Pamirs, using teleseismic receiver functions generated from locally deployed seismometers, closer to our estimate (Figure 7 of main text). Schneider (2014) also mentioned that due to complex subduction process in the Pamirs, many previous studies have mistaken Moho as a lower crustal layer, hence underestimating it.